

RESEARCH ARTICLE

Sediment-laden sea ice in southern Hudson Bay: Entrainment, transport, and biogeochemical implications

D. G. Barber¹, M. L. Harasyn^{1,*}, D. G. Babb¹, D. Capelle¹, G. McCullough¹, L. A. Dalman¹, L. C. Matthes¹, J. K. Ehn¹, S. Kirillov¹, Z. Kuzyk¹, A. Basu¹, M. Fayak^{1,2}, S. Schembri³, T. Papkyriakou¹, M. M. M. Ahmed⁴, B. Else⁴, C. Guéguen⁵, C. Meilleur⁵, I. Dmitrenko¹, C. J. Mundy¹, K. Gupta¹, S. Rysgaard^{1,6}, J. Stroeve^{1,7}, and K. Sydor⁸

During a research expedition in Hudson Bay in June 2018, vast areas of thick (>10 m), deformed sediment-laden sea ice were encountered unexpectedly in southern Hudson Bay and presented difficult navigation conditions for the Canadian Coast Guard Ship Amundsen. An aerial survey of one of these floes revealed a maximum ridge height of 4.6 m and an average freeboard of 2.2 m, which corresponds to an estimated total thickness of 18 m, far greater than expected within a seasonal ice cover. Samples of the upper portion of the ice floe revealed that it was isothermal and fresh in areas with sediment present on the surface. Fine-grained sediment and larger rocks were visible on the ice surface, while a pronounced sediment band was observed in an ice core. Initial speculation was that this ice had formed in the highly dynamic Nelson River estuary from freshwater, but $\delta^{18}\text{O}$ isotopic analysis revealed a marine origin. In southern Hudson Bay, significant tidal forcing promotes both sediment resuspension and new ice formation within a flaw lead, which we speculate promotes the formation of this sediment-laden sea ice. Historic satellite imagery shows that sediment-laden sea ice is typical of southern Hudson Bay, varying in areal extent from 47 to 118 km² during June. Based on an average sediment particle concentration of 0.1 mg mL⁻¹ in sea ice, an areal extent of 51,924 km² in June 2018, and an estimated regional end-of-winter ice thickness of 1.5 m, we conservatively estimated that a total sediment load of 7.8×10^6 t, or 150 t km⁻², was entrained within sea ice in southern Hudson Bay during winter 2018. As sediments can alter carbon concentrations and light transmission within sea ice, these first observations of this ice type in Hudson Bay imply biogeochemical impacts for the marine system.

Keywords: Hudson Bay, Sea ice, Sediment-laden, Tidal dynamics, Sediment entertainment

1. Introduction

Hudson Bay is a large, shallow inland sea that is seasonally covered by a dynamic sea-ice cover. Beyond the coastal fringe of landfast ice, cyclonic circulation of the pack ice gives rise to a pronounced west-to-east gradient in ice thickness, with thinner, younger ice in western Hudson Bay as a result of the recurrent polynya in the area, and thicker, deformed ice covering eastern Hudson Bay as a result of convergence (Landy et al., 2017; Kirillov et al., 2020). The last summer sea ice in Hudson Bay is typically found along the southern coast and may remain until

early August before melting out (Hochheim and Barber, 2014). During the Canadian Coast Guard Ship (CCGS) Amundsen cruise in June 2018 as part of the Hudson Bay System (BaySys) study, vast areas of thick, heavily deformed, sediment-laden sea ice were encountered in southern Hudson Bay. Although the Amundsen is a capable Arctic class 3 icebreaker, we found ourselves having to back and ram, even in early summer conditions, due to the thickness and strength of this ice type.

While these are the first in situ observations of sediment-laden sea ice in Hudson Bay, similar sediment-

¹Centre for Earth Observation Science, University of Manitoba, Winnipeg, MB, Canada

²Department of Geological Sciences, University of Manitoba, Winnipeg, MB, Canada

³Laval University, Quebec City, QC, Canada

⁴University of Calgary, Calgary, AB, Canada

⁵Université de Sherbrooke, Sherbrooke, QC, Canada

⁶Aarhus University, Aarhus, Denmark

⁷University College London, London, UK

⁸Manitoba Hydro, Winnipeg, MB, Canada

* Corresponding author:
Email: madison.harasyn@umanitoba.ca

laden sea-ice types have been observed previously in nearby James Bay and Foxe Basin (Pelletier, 1986), and in several areas throughout the Arctic, including the Chukchi Sea (Barnes et al., 1982; Kempema et al., 1989; Reimnitz et al., 1993; Ito et al., 2019), Laptev Sea (Larssen et al., 1987), Sea of Okhotsk (Nomura et al., 2009), Baltic Sea (Granskog, 1999), and Central Arctic (Pfirman, 1987; Nurnberg et al., 1994). Given that this unique ice type can present hazardous conditions in a region with an active open-water shipping season (Babb et al., 2019) and impact local biogeochemical cycles within Hudson Bay in a way not previously considered (Eicken et al., 2005), an in-depth analysis of the formation, transport, and melt of sediment-laden sea ice in southern Hudson Bay is pertinent.

Sediment-laden sea ice has three main formation mechanisms: Aeolian transport, suspension freezing, and anchor rafting (Reimnitz et al., 1987; Kempema et al., 1989). Aeolian transport occurs when winds deposit fine particles (<5 μm) from land onto adjacent sea ice, including particles deposited by snow (Pfirman et al., 1989; Nomura et al., 2009). Aeolian transport is considered to be negligible in Arctic environments, with deposition rates ranging from 3.3 to 21 $\mu\text{g cm}^{-2} \text{yr}^{-1}$ (Pfirman et al., 1989). Rates of Aeolian transport are not well constrained for sub-Arctic seas. Suspension freezing occurs when frazil ice is formed rapidly in turbid waters on sediment particle surfaces (Ledley and Pfirman, 1997; Darby et al., 2011; Ito et al., 2019) or due to double-diffusion at a temperature/salinity interface (Golovin et al., 1999), both of which subsequently incorporate/aggregate suspended sediment-laden ice crystals into sea ice. This process occurs most commonly when ice forms in shallow areas of open water, as in coastal flaw leads or polynyas, where enhanced momentum transfer from the atmosphere to the ocean fosters strong water column mixing and sediment resuspension coupled with cold air temperatures that drive rapid ice growth (Pelletier, 1986; Ito et al., 2019). Finally, anchor rafting occurs when an existing ice

Table 1. Categories of sediment distribution in sea ice and ice stratigraphy, from Eicken et al. (2005). DOI: <https://doi.org/10.1525/elementa.2020.00108.t1>

Category	Description
Type 1	Sediments evenly distributed throughout upper layers; often referred to as turbid ice (Kempema et al., 1989)
Type 2	Thick layers of sediment associated with ice growth and deformation events
Type 3	Rafted and fragmented layers of clean ice for which the original voids have been filled with frazil and brash ice that contain sediment
Type 4	Distinct layers of high sediment concentrations within a turbid or frazil ice matrix
Type 5	Surface sediment patches that have accumulated during ice melt

cover entrains sediment ranging in size from silts to boulders (Reimnitz et al., 1987) through direct contact with the seafloor, due to tides or wind-induced ridging (Barnes et al., 1982; Reimnitz et al., 1987; Ledley and Pfirman, 1997; Héquette et al., 1999). The latter two mechanisms of sediment entrainment occur most frequently in waters less than 50 m deep (Reimnitz et al., 1993), similar to depths found in our study region.

Although commonly formed in coastal waters, sediment-laden sea ice can be transported great distances if released into the mobile ice pack (Kempema et al., 1989; Pfirman et al., 1990; Dethleff et al., 2000; Darby et al., 2011; Krumpfen et al., 2019). Sediment-laden sea ice from coastal flaw leads in the Beaufort and Chukchi seas has been observed over 100-km offshore (Barnes et al., 1982; Kempema et al., 1989; Reimnitz et al., 1993; Ito et al., 2019), while the Transpolar Drift Stream advects sediment-laden sea ice from flaw leads of the Laptev Sea across the North Pole to exit the Arctic Ocean through Fram Strait (Larssen et al., 1987; Wegner et al., 2017) into the Greenland Sea (Pfirman et al., 1990; Darby, 2003). Sediment-laden sea ice may not be evident from optical remote-sensing platforms during winter due to the snow cover, but as the snow and ice surface melt begins in spring, sediment concentrates at the ice surface and becomes evident from optical remote-sensing platforms (Huck et al., 2007). The concentration of sediment at the ice surface subsequently reduces the albedo and limits light transmission through the ice, modifying the local surface energy balance (Ledley and Pfirman, 1997; Light et al., 1998; Frey et al., 2001). As melt progresses, sediment is released from the ice into the ocean, providing a means for redistribution of sediment around the Arctic and export to sub-Arctic seas, thus contributing to the transport of mass, nutrients, and chemical constituents in the Arctic Ocean system (Fransson et al., 2001; Nomura et al., 2009).

Sediment-laden sea ice can be classified into five categories based on its sediment distribution and ice stratigraphy (Table 1; Eicken et al., 2005). In the Chukchi Sea, Eicken et al. (2005) observed that Types 2 and 3 were the most common, while Type 1 was the rarest, and Type 5 only appeared later in the melt season as surface melt progressed.

The seasonal ice cover of Hudson Bay is particularly conducive to the widespread production of sediment-laden sea ice. Large semidiurnal tides (up to 5.0 m at Port Nelson; Canadian Hydrographic Service) drive a dynamic coastal flaw-lead system that can extend up to 1 km from the edge of the landfast ice that forms around the periphery of the Bay (Kuzyk et al., 2008b), while periods of sustained offshore winds create several large recurrent polynyas around the Bay (Barber and Massom, 2007). Flaw leads and polynyas promote persistent new ice growth over shallow coastal waters throughout winter, while convergence of the pack ice against the landfast ice creates vast rubble fields, or stamukhi, along the landfast ice edge (Kuzyk et al., 2008b) that are prone to becoming grounded and scouring the seafloor (Reimnitz et al., 1987; Héquette et al., 1999).

While sediment-laden sea ice has not been studied in situ within Hudson Bay itself, Pelletier (1986) observed ice-rafted sediments, from clay (<0.002 mm) to boulders (>200 mm), on the seafloor throughout the Bay and ascribed their presence to ice transport from the dynamic intertidal zone along the coast. The southwest coast is believed to be an important site of sediment resuspension and lateral transport due, in part, to high erodibility of the glacial shallow-water deposits and secondarily to fluvial inputs (Kuzyk et al., 2009). Although representing only a small fraction of sediment resuspension (ca. 10%), the fluvial sediment supply to Hudson Bay is strongest in the south. Indeed, the Nelson, Hayes, and Severn rivers in southwest Hudson Bay have the highest suspended sediment concentrations of the Bay's rivers (Godin et al., 2017) and provide an estimated one third of the total sediment flux to the Bay (Kuzyk et al., 2009). This southwestern area corresponds to the Hudson Bay lowlands: an area of low-relief water-saturated soils, generated from the retreat of the Laurentide ice sheet (Abraham and Keddy, 2005). The lower reaches of the lowland rivers lie in deep valleys incised into the lowlands, with near-vertical, permanently frozen river banks that will be destabilized increasingly as permafrost thaws (Rosenberg et al., 2005; Godin et al., 2017). The combination of near freezing, turbid, sediment-rich freshwater containing frazil ice being released at the mouth of the Nelson River into a dynamic marine environment, with temperatures below the freshwater freezing point, creates a unique situation where previous in situ observations have documented large, rubble fields of fresh ice. Furthermore, hydroelectric regulation upstream on the Nelson River has altered the hydrography and increased freshwater discharge during winter (Déry et al., 2011). Based on these observations, our preliminary assessment was that the large sediment-laden sea-ice floes that the Amundsen encountered were rubble fields of freshwater ice from the highly dynamic Nelson River. Using a mix of in situ and remotely sensed observations, we determine that the ice was, in fact, of marine origin, provide the spatial extent and mechanisms of formation of this ice, and comment further on the transport of this unique ice type in southern Hudson Bay and its potential biogeochemical impact on the marine environment.

2. Methods

2.1. In situ data collection

Over the period May 25 to July 13, 2018, the Canadian research icebreaker CCGS Amundsen conducted the first survey of Hudson Bay while the ice cover was still intact and freshwater runoff (i.e., freshet) was near its annual peak for unregulated waters (Déry et al., 2011). The research cruise was conducted as part of the BaySys project that focused on the effects of climate change and hydroelectric regulation of freshwater-marine coupling in Hudson Bay (BaySys Collaborators, 2018); further details on the project are available through other papers in the BaySys special feature in *Elementa*. The Amundsen was outfitted to sample a suite of physical and biogeochemical variables across the ocean–sea-ice–atmosphere interface.

During the 6-week survey, the Amundsen encountered sediment-laden sea ice, unique to southern Hudson Bay, which was thicker and far more difficult to navigate than the ice cover in other areas of the Bay (**Figure 1**). The area was comprised of predominantly sediment-laden sea-ice floes with a heterogeneous visible sediment cover at the surface, and visibly sediment-free ice floes interspersed within the ice cover. Sea-ice floes were in an advanced stage of ice melt, with large melt ponds spanning the surface and a minimal snow cover present (**Figure 1**). Sea-ice samples were collected with a Kovacs Mark II ice-coring system (9 cm diameter) from one visibly clean (sediment-free) ice floe at station 32 and one visibly sediment-laden floe at station 34 of the BaySys cruise (**Figure 2**). Two cores were collected on the same floe at station 34: One core was in an area with sediment present on the ice surface, and the other core was in an area with no sediment present on the ice surface (**Figure 1C**).

Due to time constraints, only the top meter of the ice was cored at both locations for the sediment-laden floe (station 34), whereas the full ice thickness was cored for the clean ice floe (station 32). This top meter was sampled for a vertical profile of temperature, salinity, total suspended solids (TSS), $\delta^{18}\text{O}$, and dissolved inorganic carbon (DIC). Note that TSS was only sampled for the top 0.5 m on the sediment-laden floe. A sample of the sediment at the surface of the sediment-laden floe was collected and stored for later analysis. A DJI Mavic Air remotely piloted airborne system (RPAS) was used to survey the study area and map the aerial extent and surface elevation of the visibly sediment-laden sea-ice floe (station 34). Digital elevation models (DEMs) and orthomosaics were generated from RPAS imagery using Pix4D® image-processing software. Additionally, ice beacons were deployed on several sediment-laden sea-ice floes in mid-June, which tracked the motion of these floes until they melted out in late-July.

Continuous records of temperature, salinity, and fluorescent dissolved organic matter (fDOM) were collected along the Amundsen cruise track by a thermosalinograph seawater system and WETLabs ECOFLD sensors (370 nm excitation, 460 nm emission; Guéguen et al., 2015) installed along a water intake line at 7-m depth. Continuous underway samples were validated against discrete samples collected every 12 h in amber-glass vials with little to no headspace and stored at 4 °C until analyzed for fDOM in the laboratory. Lower beam transmission was collected by the ship's rosette using a WetLabs C-star (CST558DR) transmissometer, measured at 657 nm.

Prior to the 2018 Amundsen cruise, other BaySys field programs took place during fall 2016 and winter 2017, resulting in the collection of complementary data (Hornby et al., 2016; Babb et al., 2017) that are also presented in this work. A short marine survey in fall 2016 aboard the CCGS Des Groseilliers involved water sampling across southern Hudson Bay, from the Nelson River estuary to the mouth of James Bay, for physical analyses. During winter 2017, both water and ice samples were collected for physical analyses from the stable, yet heavily deformed, landfast ice cover near the Nelson River estuary

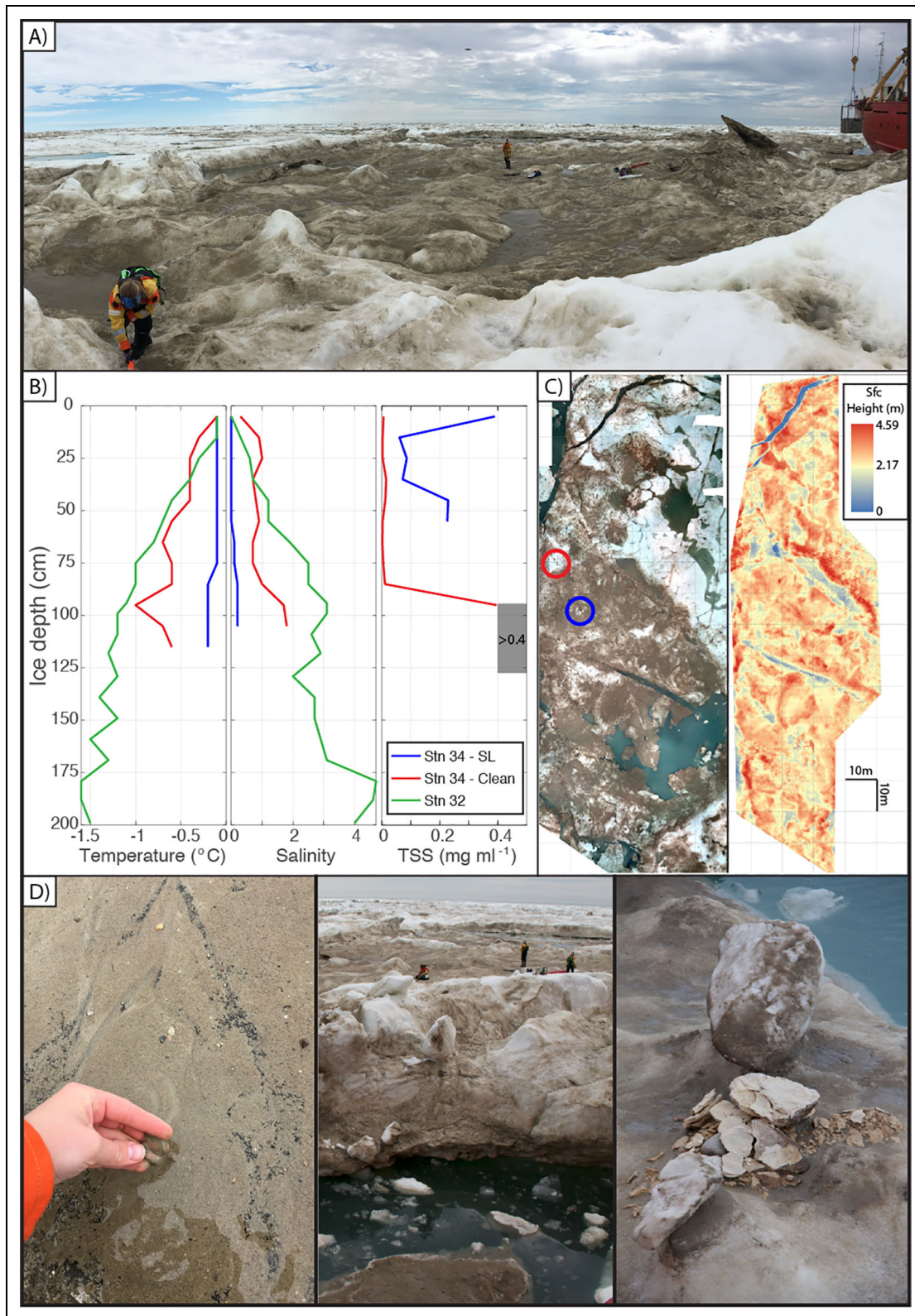


Figure 1. In situ observations of the sediment-laden (SL) sea ice. (A) Panorama over an SL sea-ice floe (station 34; **Figure 2**). (B) Profiles of temperature, salinity, and total suspended solids (TSS) from three ice cores: two from the SL sea-ice floe (station 34), one clean and one SL at the surface, and one from the clean ice floe (station 32). The gray box denotes ice sections with TSS > 0.4 mg ml⁻¹; TSS in the clean ice core was negligible. (C) Mosaic of the SL sea-ice floe (station 34) derived from imagery using a remotely piloted airborne system and digital elevation model, indicating the location of the two ice cores (clean, red circle; sediment laden, blue circle). (D) Examples of the SL sea-ice conditions (station 34). DOI: <https://doi.org/10.1525/elementa.2020.00108.f1>

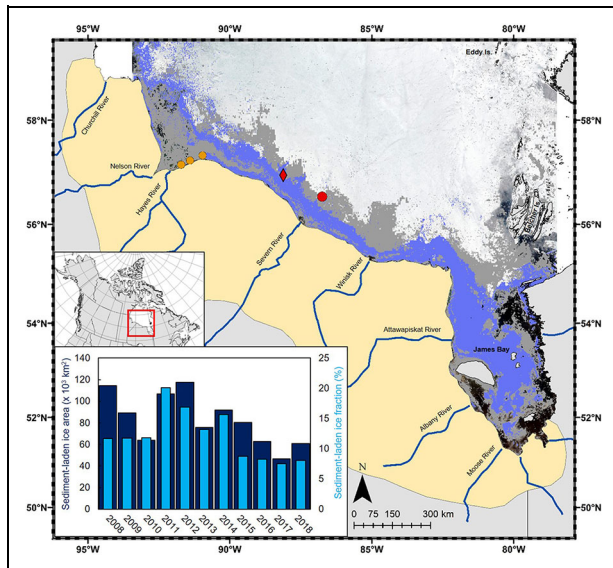


Figure 2. Spatial extent of sediment-laden sea ice in southern Hudson Bay and James Bay. Moderate Resolution Imaging Spectroradiometer imagery over southern Hudson Bay and James Bay from June 10, 2018, presenting areas classified as sediment-laden sea ice in 2018 (purple) and the cumulative spatial distribution of sediment-laden sea ice from 2008 to 2017 (gray) within the extent of displayed imagery. The inset graph shows the total area of sediment-laden sea ice (dark blue) and the fraction of the regional ice cover that is classified as sediment-laden sea ice (light blue) during June over the past decade. Location of ice sampling in 2018 near station 34 is denoted by a red dot and at station 32, by a red diamond; ice sampling completed in winter 2017 is denoted by orange dots (left to right; T1, T2, and T3). Extent of Hudson Bay lowlands is shown in light yellow. DOI: <https://doi.org/10.1525/elementa.2020.00108.f2>

and upstream along the Nelson and Hayes rivers. During the same winter field program, short-term mooring deployments were established at three sites along the landfast ice cover (T1, T2, and T3; **Figure 2**) and recorded temperature, salinity, turbidity, current velocity, and bottom pressure from February to April 2017. Turbidity was measured with an RBR XR-420 at 2.3 (T1), 0.4 (T2), and 0.5 m (T3) below the ice, while the bottom-mounted RBR solo sensors were deployed at a mean depth of 3.8, 4.9, and 7.3 m, respectively. Due to a large semidiurnal tide and a relatively low position of the turbidity sensor at T1, the sensor dropped periodically to the seafloor; the data associated with these periods were removed. Under-ice velocities were measured by a downward looking Nortek Aquadopp Z-cell 600 KHz current profiler.

2.2. Discrete water and ice chemistry

Water samples collected during the campaigns of fall 2016, winter 2017, and spring 2018 were analyzed for DIC, total alkalinity (TA), oxygen isotopes ($\delta^{18}\text{O}$), and salinity. Samples were collected with the ship's rosette or manually using a Niskin bottle or submersible pump (Wattera

WSP-12V-1 Cyclone). Water from the Niskin bottle and submersible pump was transferred to sample vials using gas-tight tubing. Ice cores were cut into 10-cm sections and vacuum-sealed in gas-tight polyethylene bags (Cabela, 4-mm thick) to prevent air contamination, then melted overnight at 4 °C. Once melted, the bags were opened and subsampled using a 50-mL glass syringe with a piece of flexible gas-tight tubing on the end. In all cases, water samples were collected and subsampled without introducing air bubbles.

The $\delta^{18}\text{O}$ isotopic composition of ice and water was measured at multiple sites during the spring 2018 cruise, as well as during previous BaySys expeditions in coastal southern Hudson Bay (fall 2016 and winter 2017). Oxygen isotopic measurements combined with salinity are used to distinguish meteoric water (terrestrial runoff and precipitation) from the other main freshwater source in polar oceans: sea-ice melt (Redfield and Friedman, 1969; Tan and Strain, 1996). We used our data to define end-member properties for seawater (salinity = 32.75; $\delta^{18}\text{O} = -2.25$) and for meteoric water (from river water samples; salinity = 0.01; $\delta^{18}\text{O} = -14.0$); for sea-ice melt, we used the end member of Granskog et al. (2009; salinity = 5.0, $\delta^{18}\text{O} = 0.0$). Subsamples for $\delta^{18}\text{O}$ analysis were collected in 2-mL borosilicate glass vials with polytetrafluoroethylene septa (Fisherbrand 03-391-18) or 13-mL polypropylene centrifuge tubes (Sarstedt 60.541.003). Vials were filled without headspace, wrapped in parafilm, and stored at 4 °C until analysis by Picarro L2140i at the University of Washington Isolab (O'Keefe and Deacon, 1988). Results are reported relative to Vienna Standard Mean Ocean Water. This method gives a precision of <0.1 %.

Ice-core subsamples for DIC and TA were collected following the methods of Geilfus et al. (2015). Samples were collected in 10-mL glass exetainer vials, preserved with HgCl_2 , and stored at 4 °C in the dark. Samples were analyzed for DIC using a TCO_2 autoanalyzer (AS-C#, Apollo SciTech) via sample acidification ($\text{H}_3\text{PO}_4^{3-}$) and subsequent nondispersive infrared CO_2 detection (LI-7000) with a precision of $2 \mu\text{mol kg}^{-1}$. TA was measured using potentiometric titration (Haraldsson et al., 1997) with a precision of $\pm 3 \mu\text{mol kg}^{-1}$. DIC and TA results were calibrated using certified reference material from A. G. Dickson at the Scripps Institution of Oceanography.

Samples for salinity were transferred to 125-mL glass bottles and measured using a Salinometer (GuildlineAutosal 8400B) with a precision of <0.001. The instrument was calibrated using IAPSO Standard Seawater each day.

2.3. Sediment analysis

TSS concentrations were estimated by vacuum-filtering the entire melt volume of the ice-core sections, using preweighed Whatman™ GF/F (0.7- μm nominal pore size) 47-mm diameter glass fiber filters. The filtrated samples were dried at 55 °C for 24 h prior to weighing. This process was repeated three times for a complete loss of moisture content of the filter paper and filtrate. The volume-normalized cumulative difference of filter paper weights with and without filtered sediment of all sections of an ice

core represented its bulk TSS concentration (American Public Health Association, 2005; American Society for Testing Materials, 2007). Surface sediment samples were collected on the visibly sediment-laden floe (station 34) and analyzed for particle size distribution using a Microtrac™ Particle Size Analyzer: S3500.

Mineral composition of sediment samples from the ice were compared to other samples of clean sea ice collected during the 2018 cruise in central Hudson Bay and the tidal flats in southern Hudson Bay using X-ray diffraction analysis to ascertain the provenance of the observed sediments. Oriented smear mounts were made by finely crushing and grinding the samples in a mortar and pestle, centering the powdered sample on a glass slide, and adding several drops of ethanol to spread the wet slurry across the slide with a needle tool. A Siemens D5000 powder diffractometer, scanning 6° – 66° (diffraction angle 2θ), with Cu K α radiation, at a step size of 0.02° and a scan speed of 1 s, was used to analyze the material. The spectra were interpreted off-line using Materials Data Incorporated (2012) Jade mineral identification software.

2.4. Remote sensing and reanalysis data

Moderate Resolution Imaging Spectroradiometer (MODIS) imagery (250 m spatial resolution) was obtained from the NASA EOSDIS Worldview site (<https://worldview.earthdata.nasa.gov/>) for the southern coastal region of Hudson Bay and James Bay for the past 10 years (2008–2018) during early June (**Figure 2**). A MODIS image was also retrieved for 2019 for comparison with Ice, Cloud and Land Elevation Satellite (ICESat-2) freeboard data (Section 4.1). Image dates were chosen based on the lowest cloud coverage, ranging from June 5 to June 17. Land area was clipped from all images, and a supervised classification was completed in ArcMap 10.5 specifying 5 classes: open water, turbid water, rubble ice, sediment-laden sea ice, and clean ice. Supervised classification methods and reflectance spectra of surface types were based on those provided in Rösler et al. (2012) and Huck et al. (2007). Fractional reflectance values in the optical channels (red: 620–670 nm, green: 545–565 nm, and blue: 459–479 nm) for each class type were input into the classification algorithm manually (open water, sediment-laden sea ice, and clean sea ice) or, if not presented previously in the literature, selected from an area of known class cover in the MODIS imagery (turbid water and rubble ice). Initial class fractional reflectance values were specified using imagery for the year with the clearest distinction between class areas (2018). Delineation of the five classes in the optical bands is governed by the albedo of these surface types and the proportional reflectance in the red, green, and blue wavelengths, as outlined in Huck et al. (2007). Area totals were calculated for each class, and the ratio of sediment-laden sea ice to all ice classes was determined. Sediment-laden sea-ice fractional areas were calculated using the boundary provided in **Figure 2** for total ice area.

To contrast the thickness and roughness of sediment-laden sea ice from clean sea ice, ice freeboard data collected by the ICESat-2 (Kwok et al., 2019a) during winter

and spring 2019 were analyzed. Note that ICESat-2 was launched in fall 2018, so there are no coincident data to our in situ observations. Instead, monthly gridded fields of sea-ice freeboard during winter 2019 were analyzed, while a specific profile through southern Hudson Bay during June 2019 was partitioned between sediment-laden and clean ice types from a classified MODIS image. ICESat-2 houses a laser altimeter that counts individual photons to measure elevation along three pairs of strong and weak beams. In ice-covered waters, ICESat-2 provides estimates of freeboard by defining the mean sea-surface height within approximately 10 km along track windows and then determines the elevation of the sea ice or snow surface relative to the sea surface. The sea-ice freeboard data set ATL10/L3A was acquired from the National Snow and Ice Data Center and provides sea-ice freeboard estimates at approximately 15 m resolution along the strong beams (Kwok et al., 2019b).

Weekly ice charts produced by the Canadian Ice Service were used to determine the average width of landfast ice along the southern shore of Hudson Bay (Nelson River to James Bay) during winter (January–March) between 2010 and 2019. Based on expert manual interpretation of remotely sensed imagery, and in situ and airborne observations, ice charts delineate different ice regimes with polygons according to the World Meteorological Organization egg code. Landfast ice polygons were used to calculate the width of the landfast ice at 100-km intervals along the southern shore and provide a measure of the average landfast ice conditions during winter.

Given the absence of in situ observations of sea-ice melt from the area of sediment-laden sea ice, the onset of surface melt was inferred from the seasonal time series of air temperatures from the nearby Environment Canada station at Fort Severn, Ontario (https://weather.gc.ca/canada_e.html) and the ERA-5 (ECMWF re-analysis; Copernicus Climate Change Service Climate Data Store, 2017) point nearest to the sediment-laden sea-ice site. Environment Canada observations were collected hourly with an automated weather tower near the community of Fort Severn, which is located near the mouth of the Severn River (**Figure 2**). ERA-5 provided 2 m air temperatures at 6-h intervals.

3. Results and discussion

3.1. Extent and physical properties of sediment-laden sea ice

Relative to the ice cover encountered by the Amundsen in other regions of Hudson Bay, the sediment-laden sea ice along the southern Hudson Bay coast was much thicker and nearly impassable even with the icebreaker. The sediment-laden sea ice was heavily deformed with extensive ridges and hummocks that created a very rough ice surface with some features extending 4.6 m above sea level (**Figure 1**; Harasyn et al., 2019). The extreme thickness of the ice prohibited the physical measurement of ice thickness, although an RPAS-generated DEM of the visibly sediment-laden sea ice floe (approximately 200×100 m, station 34) revealed an average freeboard of 2.2 m (**Figure 1**), which, assuming an ice density of 930 kg m^{-3} (Timco

and Weeks, 2010), corresponds to a total ice thickness of 18 m in hydrostatic equilibrium. In comparison, ice thickness at all of the other BaySys stations located across the Bay ranged from 0.46 to 2.65 m.

While operating within the sediment-laden sea ice area in southern Hudson Bay, all five forms of sediment-laden sea ice defined by Eicken et al. (2005) were observed, with particularly noteworthy sediment bands in broken or turned-over floes (Types 2–4) and considerable sediment accumulation at the surface of the ice floe (1–2 cm thick, Type 5; **Figure 1**). In situ observations revealed that the top meter of the ice was isothermal and fresh, which in combination with the observed accumulation of sediment at the ice surface (**Figure 1**) indicates that ice melt was underway. Interestingly, the ice core collected from an area with 1–2 cm of sediment at the surface (station 34 sediment-laden site; **Figure 1**) was notably warmer and fresher than the ice cores collected where no sediment was present at the surface (station 32, station 34 clean site; **Figure 1**), which leads us to infer that increased absorption of solar radiation by dark sediments on the sea ice surface had enhanced surface melt and brine drainage. The two cores taken from the same sediment-laden floe had differing temperature and salinity profiles, suggesting that the effects from increased absorption of solar radiation are localized to areas immediately underneath sediment.

The sediment profiles from the two ice cores collected at the sediment-laden and clean sites of the same ice floe were quite different (**Figure 1B**). The profile from the visibly sediment-laden site had a peak sediment concentration of 0.4 mg mL^{-1} at the surface but declined to values between 0.08 and 0.22 mg mL^{-1} at 0.5 m. Conversely, the surface-clean site had low sediment concentrations through the upper 0.85 m but a pronounced sediment band below, with sediment concentrations exceeding 0.4 mg mL^{-1} at 1 m. The observed sediment concentrations align with the range of 0.03 – 0.6 mg mL^{-1} presented by Reimnitz et al. (1993) from sea ice in the Chukchi Sea. Analysis of particle size of sediment found within the ice ranged from 9 to $415 \text{ }\mu\text{m}$, while larger particle aggregates and rocks as large as golf balls (40-mm diameter) were evident on the surface (**Figure 1**). The observed particle size distribution indicates that the sediment was entrained within this ice through a combination of suspension freezing (fine sediments) and anchor rafting (larger sediments and rocks).

At the time that we encountered the sediment-laden sea ice in southern Hudson Bay, it covered approximately $52,000 \text{ km}^2$, or 8% of the remaining sea-ice area (landfast and pack ice) in southern Hudson Bay, and extended in a narrow band from Cape Churchill to James Bay (**Figure 2**). Comparatively, over the last decade, sediment-laden sea ice has on average covered $64,289 \text{ km}^2$ (\pm standard deviation of $18,119 \text{ km}^2$, $n = 11$) or 12.2% ($\pm 4.1\%$) of the remaining ice cover during early June, ranging in areal extent from 47 to 118 km^2 (**Figure 2**). While the narrow band of landfast ice in southern Hudson Bay is typically sediment-laden, the historic extent of sediment-laden sea ice within the mobile pack ice is highly variable (gray

shading in **Figure 2**). The presence of sediment-laden sea ice is particularly pronounced in James Bay (**Figure 2**), which is a relatively large (about $68,000 \text{ km}^2$) and shallow (mean depth of approximately 25 m) southern extension of Hudson Bay with high riverine inputs and tidal and sea-ice conditions similar to southern Hudson Bay.

3.2. Mineralogical characteristics of sediment-laden sea ice

Analysis of filtered samples from the sediment-laden sea ice (station 34) and the tidal flats near the Nelson River estuary (**Figure 3**) reveal that all samples contain albite, anorthite, and quartz. These minerals are consistent with an igneous (diorite-granodiorite) source for the sediments and the Precambrian geology of the region (Desharnais, 2004). In addition, they contain calcite and dolomite, which is consistent with a dolomitic limestone source and the Silurian and Devonian geology of the Hudson Bay lowlands (Lavoie et al., 2015; light yellow shading in **Figure 2**). Therefore, we infer that sediment from the tidal flats is the source of the sediment observed on and within the ice in southern Hudson Bay.

3.3. Source waters of sediment-laden sea ice

Our initial in situ observations of the thickness, low salinity, and relative hardness of the sediment-laden sea ice led our field teams to presume initially that this ice was rubbled freshwater ice that we had observed previously near the mouth of the Nelson River. To further consider the potential source waters of this sediment-laden sea ice, we used $\delta^{18}\text{O}$ measurements from both water and ice collected during the various BaySys field campaigns (**Figure 3**). Ice formation preferentially retains heavy oxygen isotopes, causing ice to have a $\delta^{18}\text{O}$ value 1.5%–2.6% higher than the water from which it formed (Macdonald et al., 1995; Toyota et al., 2013; Moore et al., 2017). The $\delta^{18}\text{O}$ value of sediment-laden sea ice (-0.9%) is approximately 2% higher than seawater in southern Hudson Bay (-3.0%) and 11% higher than water from the Nelson River (-12.6% ; **Figure 3**). Similarly, Nelson River ice is approximately 2% higher than Nelson River water and much more negative than southern Hudson Bay water or sediment-laden sea ice. Landfast ice collected from the Nelson River estuary during winter 2017 has a $\delta^{18}\text{O}$ signature between that of Nelson River ice and sediment-laden sea ice. Therefore, we conclude that the sediment-laden sea ice was formed from marine waters. However, the sediment-laden sea ice was very fresh (salinity = 0–1) relative to typical sea ice, suggesting that it was in an advanced stage of melt and that most of the brine had been drained.

The difficulty that the Amundsen had in breaking through this ice is counterintuitive to the notion that it was well-drained first-year sea ice. We have many examples of breaking through thick first-year and multiyear sea ice in the Beaufort Sea with the Amundsen during summer (e.g., Barber et al., 2009, 2014), yet this ice was different and presented difficult navigational conditions typical of freshwater ice formed from riverine sources. We know from the $\delta^{18}\text{O}$ analysis (**Figure 3**) that the ice sampled

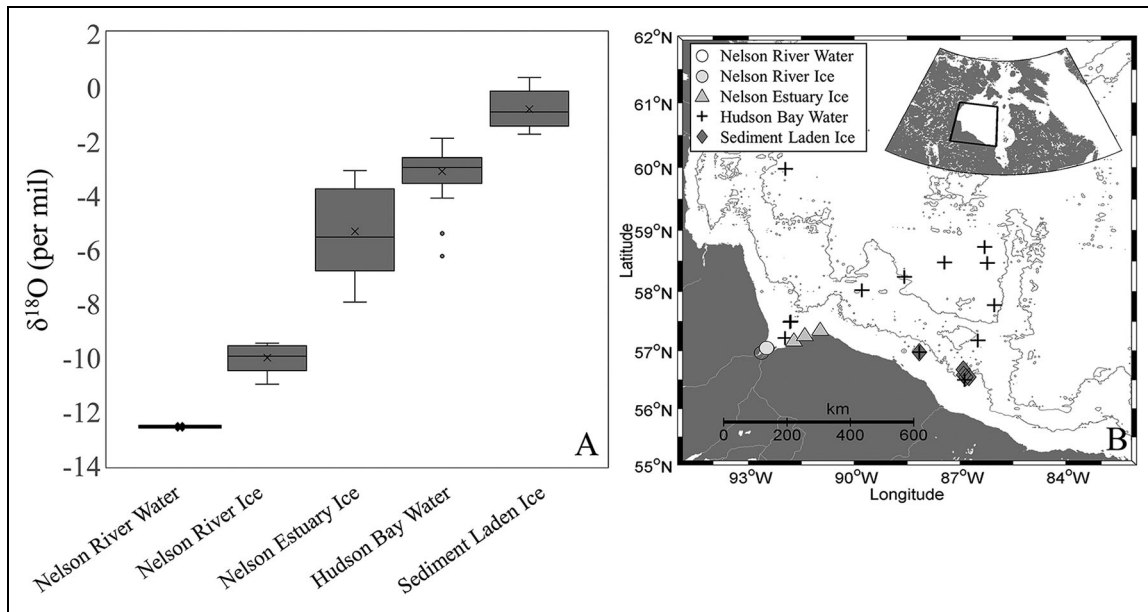


Figure 3. The $\delta^{18}\text{O}$ values for sea-ice and water samples from Hudson Bay. The box and whisker plots in Panel A show the median $\delta^{18}\text{O}$ value (horizontal line in box), interquartile ranges (upper and lower edge of each box), and mean value (x). Upper and lower whiskers denote the most positive and most negative isotope values that are within 1.5 times the interquartile range above the upper and lower quartiles, respectively. Outliers are denoted by dots outside the whiskers. Samples were collected during June 2018, except the Nelson Estuary ice samples which were collected during winter 2017 at sample locations shown in Panel B. DOI: <https://doi.org/10.1525/elementa.2020.00108.f3>

had formed from marine water, yet most of the salt had been drained by the time we sampled the floe (Figure 1C). Concentration of sediment at the ice surface shows that surface melt had occurred, and surface air temperatures for the region show that daily high air temperatures had exceeded 0 °C over 2 months prior to the date of sampling (Figure 4). Since mid-April, the region had experienced diurnal freeze-thaw cycles that would have gradually warmed the ice cover and led to both vertical and lateral brine drainage of the warming and increasingly porous ice cover (Figure 4). Additionally, the elevated freeboard of the ice floe sampled at station 34 (Figure 1) would have created a pressure head to drain brine from the upper portion of the ice as it warmed, freshening this part of the ice, which was the source of our samples. The subsequent refreezing of melt water in the ice through diurnal freeze-thaw cycles would have created a more solidified ice medium, thus explaining the difficulty of navigating through this ice.

3.4. Sediment entrainment

From our analysis, sediment-laden sea ice (1) was heavily deformed (Figure 1) and much thicker than the surrounding clean level ice, (2) had formed along the southern coast of Hudson Bay independent of large rivers (Figure 2), (3) contained sediment similar to that found on the tidal flats of southern Hudson Bay, and (4) had formed from marine waters (Figure 3). The combination of these observations leads us to speculate that the sediment-laden sea ice observed in southern Hudson Bay formed throughout winter in the tidal flaw lead that forms semidiurnally between the stable landfast ice and mobile ice pack.

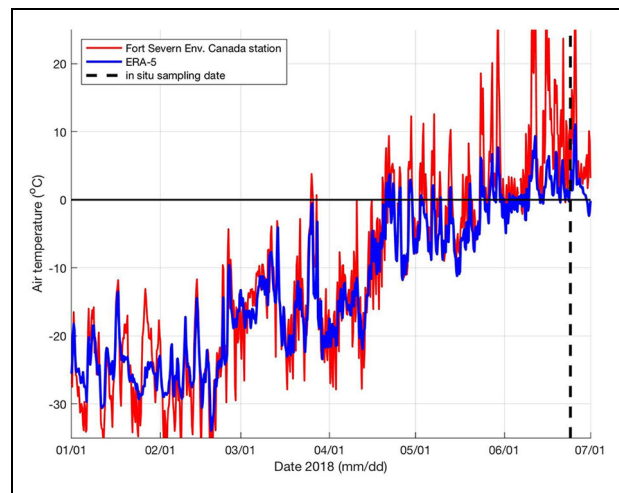


Figure 4. Air temperature time series over southern Hudson Bay. Air temperatures at 6-h intervals from the Environment Canada weather station at Fort Severn (red) and 2-m air temperatures from ERA-5 (blue) at the site of sediment-laden sea-ice sampling from January to July 2018. The vertical dashed line indicates the date of sea-ice sampling at station 34. DOI: <https://doi.org/10.1525/elementa.2020.00108.f4>

Hudson Bay is characterized by high tidal ranges and therefore strong tidal currents, which not only open the flaw lead and promote new ice growth but also drive sediment resuspension in coastal areas. In situ observations of under-ice turbidity and sea-level height collected near the landfast ice edge during spring 2017 (positions noted in Figure 2) clearly demonstrate that tidal

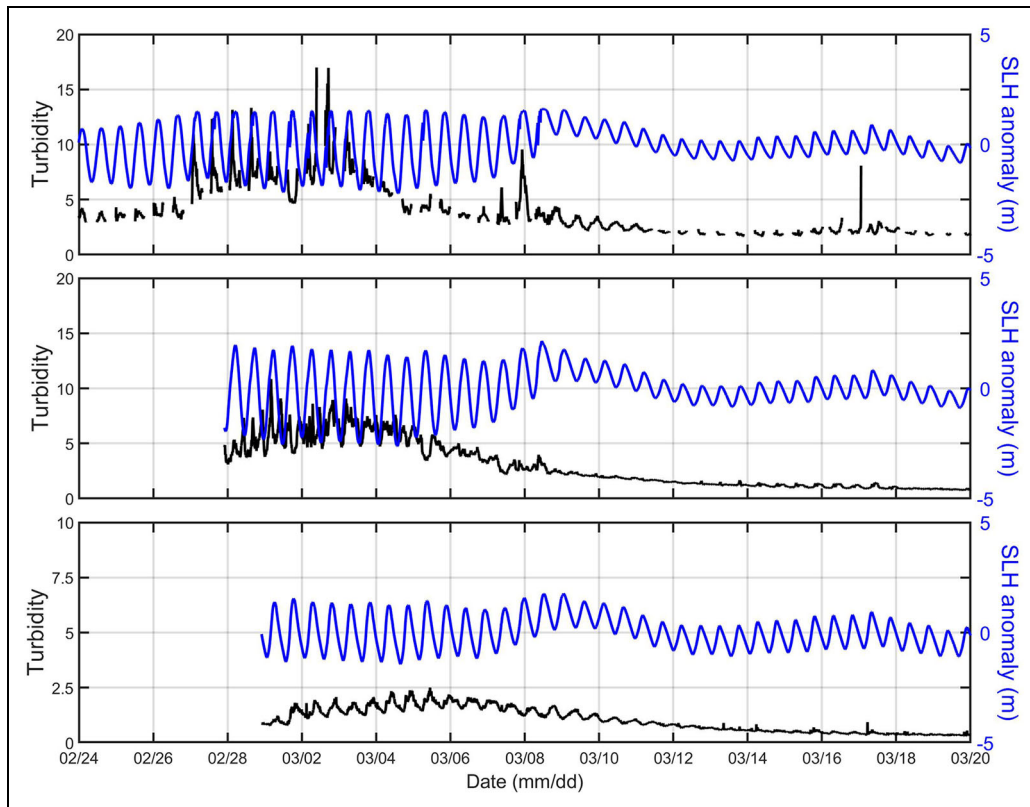


Figure 5. Mooring-retrieved under-ice turbidity and sea-level height anomaly during the BaySys spring 2017 field campaign. Panels from top to bottom correspond to locations T1, T2, and T3 in **Figure 2**. Sea-level height (SLH) anomaly is relative to the mean SLH over the record. DOI: <https://doi.org/10.1525/elementa.2020.00108.f5>

dynamics drive turbidity near the flaw lead (**Figure 5**). The observed range of sea-level height changed around a storm event on March 7–8 (coincident with other sampling done during BaySys in winter; e.g., Petrusevich et al., 2020) that compressed the pack ice against the landfast ice and extended the landfast ice cover several kilometers offshore. Prior to the storm, the tidal amplitude of 1.5–2 m was associated with observed tidal velocities greater than 0.30 m s^{-1} , whereas after the storm, the extensive landfast ice dampened the tidal signal and reduced the tidal amplitude to approximately 0.5 m and decreased tidal velocities to $0.10\text{--}0.15 \text{ m s}^{-1}$. Tidal velocities prior to the storm were above the critical threshold of 0.20 m s^{-1} , which Miller et al. (1977) identified as the threshold to resuspend silty sediments with a mean grain size of 0.018 mm. This size is on the lower range of our observed particle size analysis (0.009–0.415 mm). After the storm, the dampened tidal velocities were insufficient to resuspend sediment, leading to reduced turbidity at the mooring sites. However, we presume that tidally driven turbidity still occurred along the new landfast ice edge, albeit in slightly deeper waters, and continued to promote sediment resuspension near the flaw lead.

Tidal dynamics make the flaw lead a very dynamic sea-ice environment, creating heavily deformed and thick pieces of ice (approximately 18 m, from RPAS-calculated elevations) that either remain grounded within the stamukhi or are advected within the mobile ice pack. Remotely sensed fields of ice thickness do show an increase in ice

thickness in southern Hudson Bay, but the mean ice thickness during March varied from 1.5 to 2 m in southern Hudson Bay and ice thickness distributions over this area do not show the presence of very thick ice (Landy et al., 2017). This apparent absence of very thick ice may be the result of the relatively coarse along-track resolution of CryoSat-2 (200 m) or the filtering that was applied to remove such elevated freeboards as erroneous values. Examining sea-ice freeboard as measured by the more recent satellite altimeter ICESat-2, which has an along-track resolution of 14 m (Kwok et al., 2019a), reveals considerably higher sea-ice freeboards along the southern coast of Hudson Bay during the winter of 2019 (**Figure 6**). Monthly maps of the gridded sea-ice freeboard reveal the seasonal increase in freeboard as the ice cover grows thicker during winter, as well as the pronounced west–east gradient in ice thickness across Hudson Bay first identified by Landy et al. (2017). The southern Hudson Bay area routinely had the greatest freeboards within the Bay in winter 2019, and the spatial extent of the higher freeboards expanded throughout the season, as expected if the deformed ice was transported both along- and offshore under the Hudson Bay cyclonic circulation pattern.

A more detailed analysis of an ICESat-2 track from June 18, 2019, where we distinguished between sediment-laden sea ice (blue shading) and sediment-free pack ice, revealed a considerable difference in freeboard between the two ice environments. The modal draft of the sediment-laden sea ice (16 cm) was more than twice that of the sediment-free

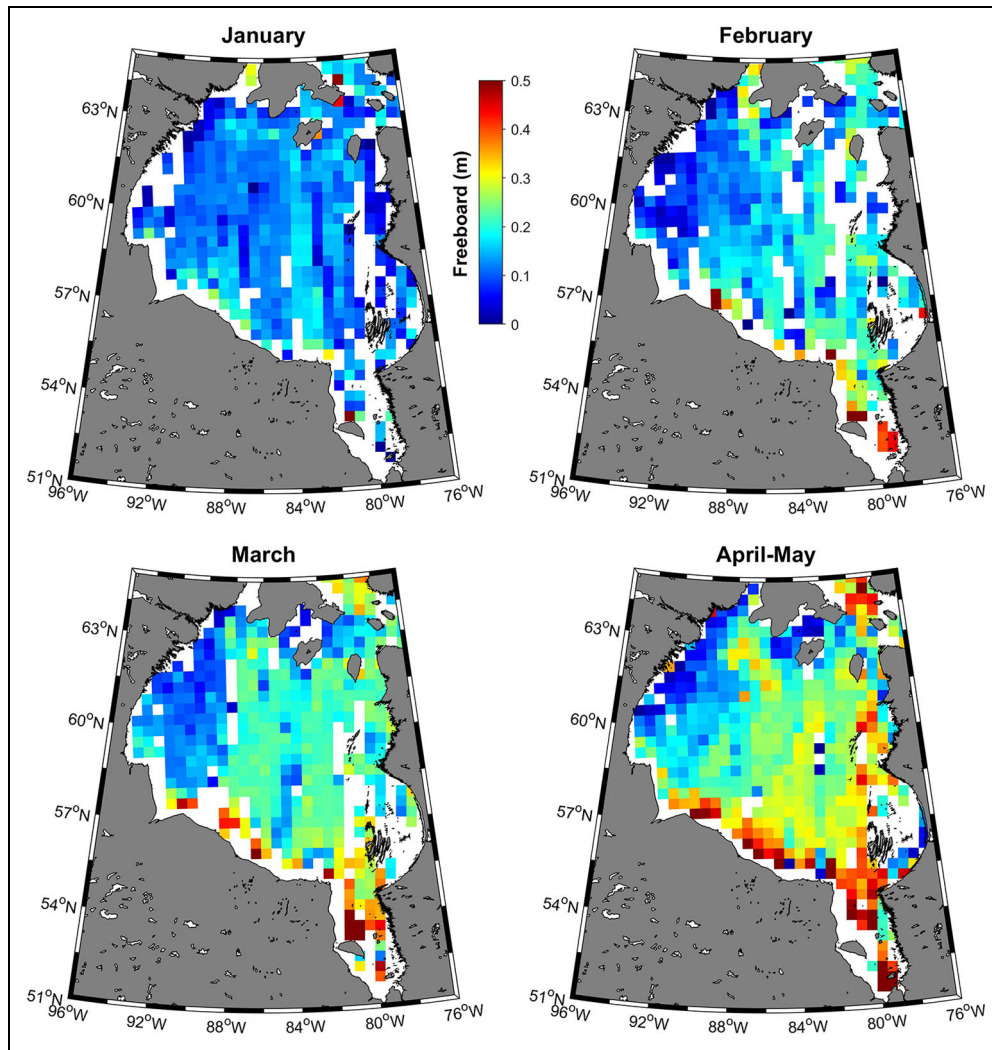


Figure 6. Monthly fields of sea-ice freeboard from ICESat-2 from January to May 2019. Seasonal increase in freeboards can be seen in southern Hudson Bay and James Bay, along with the development of a west–east gradient in ice thickness. ICESat = Ice, Cloud and Land Elevation Satellite. DOI: <https://doi.org/10.1525/elementa.2020.00108.f6>

pack ice (6 cm), while the sediment-laden sea ice also had a much broader distribution (**Figure 7B**). Additionally, the sediment-free pack ice shows a secondary mode of open water, which indicates the presence of leads within a diffuse ice cover, whereas the sediment-laden sea-ice cover remained consolidated with very little open water present. ICESat-2 observations revealed that the sediment-laden sea ice was much thicker and deformed than the nearby pack ice, which, as we alluded to above, can be related to the dynamic flaw lead where this ice had formed and entrained sediment. The ICESat-2 freeboards, however, do not reflect the extreme mean freeboard of 2.2 m, which we observed at the sediment-laden floe sampled. The along-track resolution of ICESat-2 is at the length scale of these extreme features, though the ICESat-2 profiles may not have passed over such a feature, or such an extreme freeboard may have been filtered as an outlier. Either way, a more detailed analysis with the newly available ICESat-2 data sets may provide more information on the presence of extreme freeboards within coastal areas of southern Hudson Bay.

Beyond suspension freezing within the tidal flaw-lead system, there was evidence that the sediment-laden sea-ice floes encountered by the Amundsen had been grounded at one time and had also experienced ice rafting or overturning, as the accumulation of larger particles, such as rocks, on the surface cannot be explained by suspension freezing (Reimnitz et al., 1987). While grounded ice stabilizes the landfast ice cover and promotes expansion throughout winter, as we observed in March 2017, the tidal activity limits the extent of the landfast ice cover to shallow areas where the ice is anchored and water depth decreases to only a few meters during low tide. Grounded ice was observed frequently within the landfast ice during winter surveys conducted in 2017 as part of BaySys (author observations), with some areas grounding only during low tide and other larger deformed ridges remaining grounded throughout the tidal cycle. During these landfast ice surveys, the sea surface height was only 1.5, 2.5, and 6 m near the landfast ice edge at the T1, T2, and T3 transects (**Figures 2 and 6**), respectively. Furthermore, in terms of sediment supply, rivers provide a vast

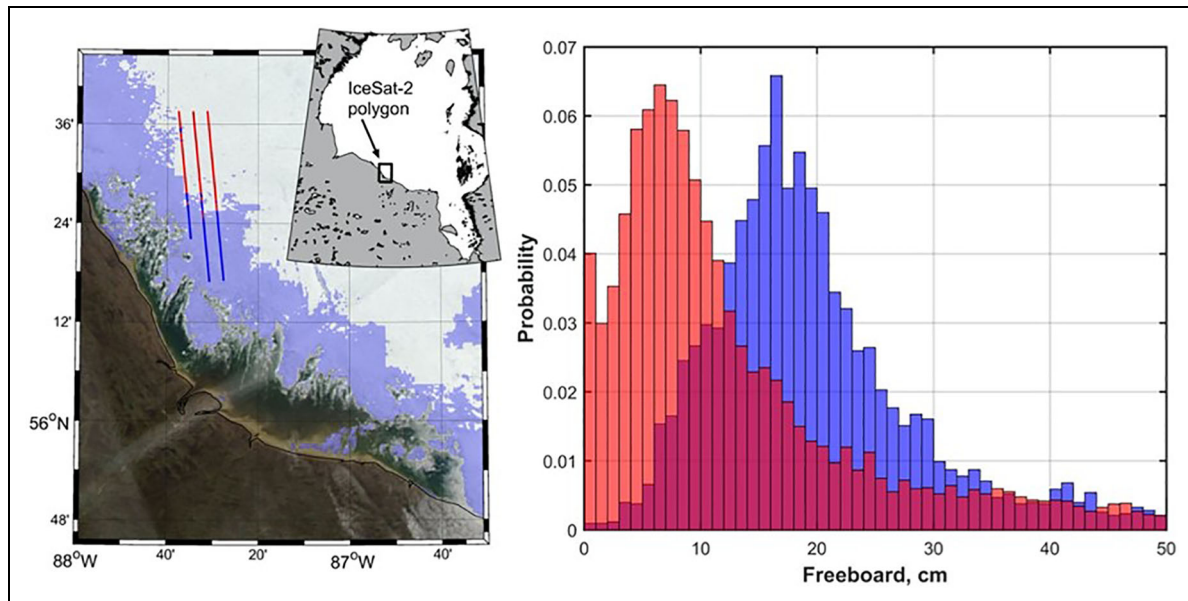


Figure 7. Sea-ice freeboard from ICESat-2 over sediment-laden sea ice on June 18, 2019. Blue area represents sediment-laden sea ice, determined from supervised classification of Moderate Resolution Imaging Spectroradiometer imagery. Track segments and probability density function bars in red represent clean ice, whereas blue track segments and probability density function bars represent sediment-laden sea ice. ICESat = Ice, Cloud and Land Elevation Satellite. DOI: <https://doi.org/10.1525/elementa.2020.00108.f7>

quantity of the sediment into the coastal areas of Hudson Bay (Kuzyk et al., 2008a) that is available for suspension freezing. Yet the marine source of the sediment-laden sea ice indicates that sediment from the rivers is only entrained within the ice once it has been mixed with marine waters or deposited and subsequently resuspended by tidal currents or during strong wind events.

Mechanisms of sediment-laden ice formation in a dynamic environment such as southern Hudson Bay are summarized as a conceptual diagram in **Figure 8**. Although the location of the landfast ice edge varies along the coast and through winter, averaging 11.33 km from shore, the tidal flaw lead opens during ebb tide as the pack ice is advected offshore, creating an environment for frazil/new ice formation in turbid waters. The width of the flaw lead represents an area for future research in Hudson Bay, but it was estimated by Kuzyk et al. (2008b) as approximately 1 km near Churchill from March to May 2005, while in situ observations during winter 2017 revealed widths ranging from hundreds of meters to several kilometers. The flaw lead reaches its maximum width during low tide and begins to close with the onset of flood tide, thereby compressing the recently formed frazil/new ice against the landfast ice edge and dynamically thickening the ice cover. This process incorporates sediment-laden frazil ice into both the landfast and pack ice. Tides also lead to grounded ice, as thicker deformed pieces are forced against the landfast ice edge and, therefore, into shallower waters during flood tide, while floes may become grounded during ebb tide if they are not advected offshore into deeper waters. Grounded ice leads to the incorporation of larger sediment from the seafloor into the bottom of grounded ice. The repetition of this cycle

through the winter and spring results in highly deformed thick sediment-laden ice both within the coastal landfast ice and in the mobile ice pack, within which sediment-laden ice may be advected both alongshore and offshore.

In terms of the total mass of sediment transported by sea ice in southern Hudson Bay, we conservatively estimated a total sediment load of 7.8×10^6 t, or 150 t km^{-2} , entrained within the sea ice of southern Hudson Bay during winter 2018. This estimate is based on our observed average sediment concentration of 0.1 mg mL^{-1} in southern Hudson Bay sea ice, an areal sediment-laden sea-ice extent of $51,924 \text{ km}^2$ in southern Hudson Bay in June 2018, and an estimated regional sea-ice thickness of 1.5 m at the end of winter (from the data presented in Landy et al., 2017). The estimated sediment load of 150 t km^{-2} is greater than that reported by Eicken et al. (2005) for the Chukchi Sea (128 t km^{-2}). It is also a conservative estimate, because not all sediment is visible at the ice surface leading to an underestimation of sediment-laden sea-ice extent (e.g., **Figure 1**).

3.5. Transport and release of sediment from sea ice

While sediment-laden sea ice is formed in the coastal tidal flaw lead, it can be advected within the mobile ice pack or transported offshore when the landfast ice cover breaks up during spring. Sediment-laden sea ice is thus a pathway for the transport and redistribution of a substantial volume of material from the tidal flats, which underlie the dynamic coastal flaw lead, to the offshore area where it is deposited during ice melt (e.g., Pelletier, 1986). Interannual variability in atmospheric forcing, and therefore ice motion (e.g., Kirillov et al., 2020), will drive variability in the transport and extent of sediment-laden sea ice which

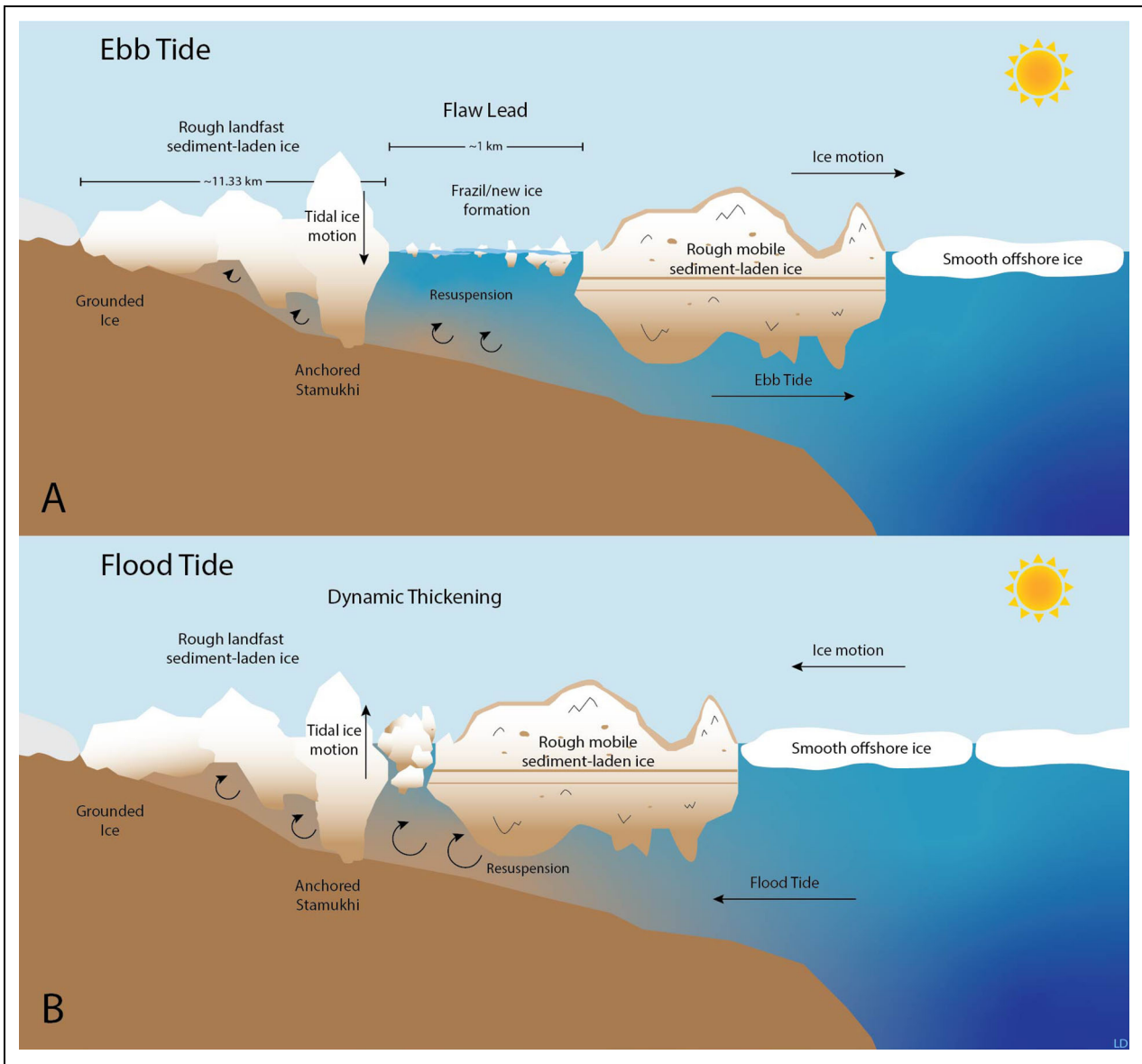


Figure 8. Conceptual diagram of sediment-laden sea-ice formation in a dynamic tidal flaw-lead environment. Sediment becomes entrained during frazil/new ice formation when the flaw lead opens (A) and becomes incorporated into larger ice floes when the flaw lead closes (B). Thick ice floes become anchored in shallow coastal waters during high tide, allowing for the incorporation of larger sediment particles from the sea floor. Horizontal scale of the flaw lead is exaggerated for display purposes. DOI: <https://doi.org/10.1525/elementa.2020.00108.f8>

in turn will affect where sediment is deposited. In situ tracking using ice beacons deployed on four sediment-laden sea ice floes from mid-June to the end of July 2018, when the ice cover melted out, revealed that the floes, although mobile, were not advected great distances. The floes drifted through tidal oscillations at speeds up to 2.5 km h^{-1} but ultimately melted out within 30 km of their initial location 6 weeks prior (data not shown). Conversely, Petrusевич et al. (2020) ascribed a peak in acoustic backscattering at a mooring in western Hudson Bay during spring 2017 to sediment being released from a melting sediment-laden sea-ice floe: The mooring was approximately 100 km offshore from the west coast of Hudson Bay and the sediment-laden sea ice had likely

formed in the coastal areas near the polynya in western Hudson Bay.

While we did not directly observe the release of sediment from melting sediment-laden sea ice, the Amundsen's underway system measured an area of low salinity waters (approximately 20) that had high fDOM (up to 9,000 counts; **Figure 9**) within one of the patches of sediment-laden sea ice encountered near station 32 by the Amundsen. This peak in fDOM was considerably greater than in the rest of southern Hudson Bay (750 counts), which was already three times greater than fDOM observations measured elsewhere in the Bay. The observed high fDOM signal was confirmed by the analysis of discrete water samples (data not shown).

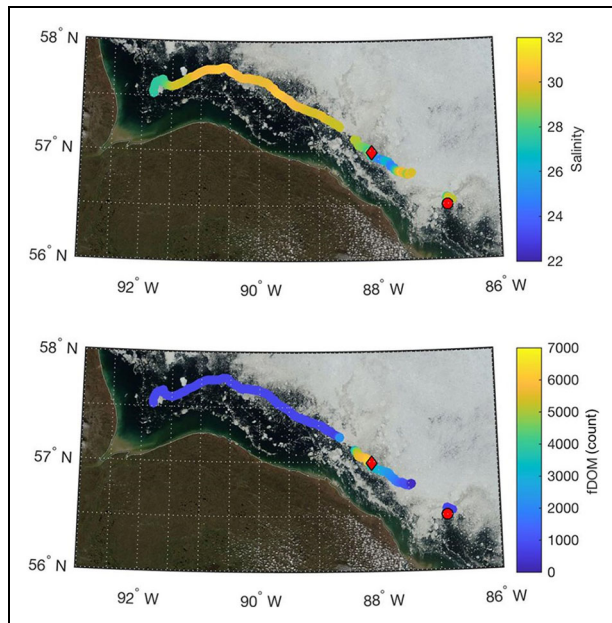


Figure 9. Underway measurements of salinity and fluorescent dissolved organic matter (fDOM) along the Amundsen's cruise track through southern Hudson Bay. Moderate Resolution Imaging Spectroradiometer image from June 18, 2018, 1 day prior to sampling at station 32 (red diamond) and 2 days prior to sampling at station 34 (red dot). Color scale indicates underway measurements for salinity (top) and fDOM (bottom). The Nelson River estuary is shown on the left-hand side of the map. DOI: <https://doi.org/10.1525/elementa.2020.00108.f9>

The high fDOM signal in these waters has several potential sources: (1) river water, (2) resuspended sediments or suspended particles, and (3) organic material released from melting sediment-laden sea ice. A river influence appears likely based on the high fraction of meteoric water (by $\delta^{18}\text{O}$ analysis) in the fDOM patch: At 10-m depth, the fraction of meteoric water was 0.12 at station 32 and 0.11 at station 34. This patch was located approximately 400 km from the Nelson River, with marine waters of lower fDOM occurring between the high fDOM patch area and the river. Additional rivers along southern Hudson Bay (e.g., Severn River) are located east of this area with their plumes transported further east under the cyclonic circulation of surface waters in Hudson Bay (Granskog et al., 2009). In the area of the high fDOM patch, we found negative values for the fraction of sea-ice melt water (-0.06 to $+0.01$) in six of the seven samples within the upper 10 m of the water column in this area (four stations total), suggesting that the patch waters were enriched in brine, a potential source of fDOM as previously observed in the western Arctic Ocean (Dainard et al., 2019). Because the Hudson Bay shelves are generally shallow, sea-ice interactions with organic-rich sediments may also be an important source of fDOM (Skoog et al., 1996; Guéguen et al., 2007), particularly during storm events, alongshore currents and ice rafting (Reimnitz et al., 1992; Eicken et al., 1997). Sediment resuspension is likely as lower beam

transmission was observed in the fDOM patch. Ultimately, these observations lead us to speculate that this patch of fDOM-rich waters was the combined result of freshwater mixing, release of brines, and melting sediment-laden sea ice and represents the next stage in the redistribution of organic carbon and sediment from the coastal flow leads to the deeper waters in southern Hudson Bay via sea ice that was first identified by Pelletier (1986).

3.6. Biogeochemical implications of sediment-laden sea ice

Beyond the formation and presence of sediment-laden sea ice, understanding how its presence may modify marine biogeochemical cycles and local radiation budgets is important. The upper 1 m of sediment-laden sea ice that we analyzed had DIC levels of $44\text{--}53\ \mu\text{mol kg}^{-1}$ and TA of $97\text{--}108\ \mu\text{mol kg}^{-1}$, both of which are lower than in sea ice from central Hudson Bay during spring 2018: $220\text{--}640\ \mu\text{mol DIC kg}^{-1}$ and $300\text{--}680\ \mu\text{mol TA kg}^{-1}$. The observed TA: DIC ratio of approximately 2:1 in the sediment-laden sea ice is typical for sea ice (e.g., Rysgaard et al., 2007), while the low concentrations could have resulted from removal of these dissolved constituents through brine drainage (consistent with the lower salinity of sediment-laden sea ice relative to central Hudson Bay sea ice) or from ice formation in seawater with lower initial concentrations of DIC and TA. On the latter, river water is typically lower in both DIC and TA relative to marine waters (Azetsu-Scott et al., 2010; Tank et al., 2012; Azetsu-Scott et al., 2014; Burt et al., 2016). Coastal waters in Hudson Bay (within approximately 100 km of the coast) contain large fractions of meteoric water (i.e., runoff, precipitation) relative to offshore waters (Granskog et al., 2009; Burt et al., 2016). Little is known about the biogeochemistry of sea ice formed in areas heavily influenced by river discharge (Thomas et al., 2010). Runoff-influenced sea ice may be characterized by lower salinity, porosity, and ice-algal growth than typical marine sea ice (Granskog et al., 2005; Granskog et al., 2006).

Sea-ice melt can drive the marine carbonate system toward conditions of undersaturation for CaCO_3 minerals (Yamamoto-Kawai et al., 2009). This effect is particularly true for aragonite, which is used to build the shells of many marine organisms. In Arctic and sub-Arctic seas, aragonite undersaturation events can be caused by the low salinity and low DIC/TA concentrations of sea-ice melt, which dilutes CO_3^{2-} concentration. The relatively high TA: DIC ratio of the sediment-laden sea ice in Hudson Bay may offset this effect by increasing the buffering capacity of surface water; however, the vast volume of sediment-laden sea ice creates the potential for widespread (but transient) undersaturation in surface waters during the melt season. The TA: DIC ratio of sea ice is typically higher than the seawater from which it formed, due to the precipitation of calcium carbonate (ikaite) within sea-ice brine (Rysgaard et al., 2007). An additional source of high TA may be the presence of carbonate-rich sediments derived from the limestone-rich geology in the region (Fransson et al., 2020). The presence and offshore transport of carbonate minerals by sediment-laden sea ice

could alter the inorganic carbon system in offshore waters, depending on the magnitude of the carbonate load (Fransson et al., 2015). The deep offshore waters of Hudson Bay are rich in DIC, have low pH, and are undersaturated with respect to calcium carbonate (Azetsu-Scott et al., 2014; Burt et al., 2016). The low CaCO_3 saturation state could be offset, to some degree, by dissolution of the CaCO_3 supplied by sea ice. Biological processes occurring within the ice can also alter nutrients and inorganic carbon concentrations, causing the nutrients released during melt to differ from those originally incorporated during ice formation (Nomura et al., 2009). However, future work is needed to determine whether the upper 1 m we were able to analyze is representative of the entire ice profile.

A high sediment load strongly affects the optical properties of sea ice by reducing the surface albedo and by enhancing light attenuation within the sea ice and therefore affecting photosynthetic activity underneath (Light et al., 1998; Perovich et al., 1998; Frey et al., 2001; Ehn et al., 2008; Gradinger et al., 2009). Frey et al. (2001) sampled sediment-laden sea ice near Barrow, Alaska, and observed a low albedo of 0.29 and absorption of 74% of the incoming solar radiation in the uppermost centimeters of the sediment-laden sea ice. Photosynthetic organisms, such as ice algae inhabiting the sea ice, phytoplankton in the underlying water column, and microphytobenthos on the seafloor of coastal regions, rely on a sufficient transmission of light to grow and accumulate biomass, the primary food source for pelagic (water column) and benthic (seafloor) communities. Reduced light availability caused by less transparent sediment-laden sea ice could potentially inhibit or delay the onset and magnitude of spring primary production, as previously shown in a delayed ice-algal bloom in coastal Alaskan waters (Gradinger et al., 2009). Low primary production might be one of the factors contributing to the low abundance of copepods observed at station 34. Copepods, an important group of zooplankton that transfer energy up the food chain from primary producers, had a mean biomass of only 42.1 mg C m^{-2} at station 34 compared to $738.5 \text{ mg C m}^{-2}$ at sea-ice stations sampled in Hudson Bay in 2018 (S Schembri, personal communication, 2018).

A prolonged reduction in under-ice light levels (after snow melt) due to a high sediment load also has the potential to impact the development of polar cod (*Boreogadus saida*) larvae, which rely on higher light intensities to detect prey (Varpe et al., 2015). Nonetheless, polar cod were present in similar abundances among sediment-laden sea ice as elsewhere in Hudson Bay (S. Schembri, personal communication). Moreover, polar cod have been observed to hatch earlier beneath sea ice in Hudson Bay (Graham and Hop, 1995; Bouchard and Fortier, 2008), presumably due to the thermal refuge provided by fresh and brackish water at the surface (Bouchard et al., 2015). Ultimately, knowledge about how sediment-laden sea ice impacts the biogeochemical and related physical dynamics throughout the year is sparse and requires further investigation.

4. Conclusions

During a research cruise through Hudson Bay in spring 2018, the CCGS Amundsen encountered and struggled to navigate through vast areas of heavily deformed sediment-laden sea ice in southern Hudson Bay. Sediment-laden sea ice had previously been observed in James Bay and Foxe Basin, and was known to be a transport mechanism for sediment from coastal areas to the central Bay, but these are the first in situ observations in southern Hudson Bay. The difficulty of ship navigation through this ice initially led to speculation that it was freshwater ice that had formed in coastal areas of the Nelson River estuary, which had been observed previously during coastal-based surveys in winter. However, isotopic analysis revealed that this ice had formed from marine waters. Previous work has shown that sediment-laden sea ice is typically formed through either suspension freezing within flaw leads and polynyas or anchor rafting in shallow coastal areas. In southern Hudson Bay, large tides form a flaw lead semidiurnally, creating an area of open water up to 1 km wide where new ice forms rapidly and sediment is resuspended by tidal velocities. Intuitively, this dynamic coastal area presents unique conditions for expansive formation of sediment-laden sea ice through suspension freezing while also creating a deformed ice cover and agglomerate floes. These floes may become grounded, anchoring the landfast ice cover to the coast, or driven offshore into the pack ice through advection.

Within the region of sediment-laden sea ice, the ice cover was heavily deformed with layered sediment bands visible in passing floes and concentrated mattes of sediment on the ice surface indicative of sediment accumulation through surface melt. An RPAS survey determined an average freeboard of 2.2 m over one of the sediment-laden sea-ice floes, which corresponds to a mean ice thickness of 18 m. ICESat-2 observations highlighted the development of thicker ice along a coastal band in southern Hudson Bay throughout winter and also demonstrated that sediment-laden sea ice during June has a considerably greater freeboard than the nearby clean ice. Direct observations from ice cores collected on the sediment-laden sea ice revealed sediment bands below areas of “clean” surface ice and an average sediment concentration of 0.1 mg mL^{-1} . Additionally, vertical temperature and salinity profiles showed that the top meter of the ice floe was warm and relatively fresh, indicating that surface melt had begun and brine had been drained from the ice. However, given the difficulties of traveling through this area, the internal melt of the encountered sediment-laden sea-ice floes had not likely started, which could prolong hazardous shipping conditions for communities along the southern shore of Hudson Bay into the summer months.

The role of tides in the formation of sediment-laden sea ice distinguishes southern Hudson Bay from other areas of the Arctic where sediment-laden sea ice forms. Tidal amplitudes are low in both the Laptev and Beaufort/Chukchi seas, precluding the semidiurnal formation of a flaw lead where new ice production occurs. Extending the work of Reimnitz et al. (1987), we have shown that the environmental conditions that drive sediment entrainment in southern Hudson Bay differ from these other two regions

and provide a mechanism for persistent sediment resuspension and entrainment that may lead to an overall greater ice-borne sediment load than in either the Laptev or Beaufort/Chukchi Seas, where sediment is entrained episodically when large coastal polynyas form. Future research is required to confirm our proposed method of sediment ice formation and to fully understand the transport and biogeochemical impacts of sediment-laden sea ice in southern Hudson Bay.

Data accessibility statement

Data sets within this article have been archived on the Canadian Watershed Information Network (<http://lwbin-datahub.ad.umanitoba.ca>).

Acknowledgments

The authors thank the officers and crew of the Canadian Research Icebreaker, CCGS Amundsen, and Des Groseilliers for their excellence in support of this work. Additional thanks to Great Slave Helicopters and Churchill Wild who facilitated shore-based sampling programs as part of BaySys. Thank you to all collaborators of the BaySys program and Karen Wong from Manitoba Hydro for providing comments on this article. This work is a contribution to the Arctic Science Partnership (asp-net.org) and ArcticNet. Thank you to W. Gough, an anonymous reviewer, and the editor J. Deming for their constructive feedback on this article.

Funding

This work is a contribution to the Natural Sciences and Engineering Council of Canada (NSERC) Collaborative Research and Development project: BaySys (CRDPJ 470028-14) led by D. Barber (Academic PI) and K. Sydor (Industry PI). Funding for this work, including field studies, was provided by NSERC, Manitoba Hydro, ArcticNet, Ouranos, Hydro Quebec, the Canada Excellence Research Chair, and the Canada Research Chairs programs. Individual support from NSERC has been provided to D. Barber, D. Babb, D. Capelle, S. Rysgaard, C. Guéguen, and J. Ehn. Additional support was provided to A. Basu, L. Matthes, and M. Harasyn by the University of Manitoba Graduate Student Fellowship and to D. Babb by the Canadian Meteorological and Oceanographic Society.

Competing interests

The authors have no competing interests to declare.

Author contributions

- Contributed to original data acquisition: DB, MH, LD, LM, SK, DC, MA.
- Contributed to analysis and interpretation of the data: Everyone.
- Drafted this article: DB, MH, DBabb, GM, DC, LM, LD, SK.
- Revised this article: All authors.
- Approved the submitted version for publication: All authors.

References

- Abraham, KF, Keddy, CJ.** 2005. The Hudson Bay lowland, in Fraser LH, Keddy, PA eds., *The world's largest wetlands: Ecology and conservation*. Cambridge, UK: Cambridge University Press: 118–142.
- American Public Health Association.** 2005. *Standard methods for the examination of water and wastewater*. 19th edition. Washington, DC: American Water Works Association and the Water Environment Federation .
- American Society for Testing Materials.** 2007. Standard test method for determining sediment concentration in water samples. West Conshohocken, PA.
- Azetsu-Scott, K, Clarke, A, Falkner, K, Hamilton, J, Jones, EP, Lee, C, Petrie, B, Prinsenberg, S, Starr, M, Yeats, P.** 2010. Calcium carbonate saturation states in the waters of the Canadian Arctic Archipelago and the Labrador Sea. *Journal of Geophysical Research: Oceans* **115**(11). DOI: <http://dx.doi.org/10.1029/2009JC005917>.
- Azetsu-Scott, K, Starr, M, Mei, Z-P, Granskog, M.** 2014. Low calcium carbonate saturation state in an arctic inland sea having large and varying fluvial inputs: The Hudson Bay System. *Journal of Geophysical Research: Oceans* **119**: 6210–6220. DOI: <http://dx.doi.org/10.1002/2014JC009948>.
- Babb, DG, Andrews, J, Dawson, J, Mussells, O, Weber, M.** 2019. Marine transportation, in Kuzyk, ZZ, Candlish, LM eds., *From science to policy in the greater Hudson Bay marine region: An integrated regional impact study (IRIS) of climate change and modernization*. Quebec City, Canada: ArcticNet: 341–377.
- Babb, DG, Landy, JC, Zilinski, N, Deslongchamps, G, Matthes, L, Dalman, L, Capelle, DW, Geilfus, N, Munson, K.** 2017. Field Report: Churchill River and mobile ice survey February. Available at https://umanitoba.ca/faculties/environment/departments/ceos/media/BAYSYS_Churchill_FieldReport_2017.pdf. Accessed 15 June 2020.
- Barber, DG, Galley, R, Asplin, MG, De Abreu, R, Warner, KA, Pučko, M, Gupta, M, Prinsenberg, S, Julien, S.** 2009. Perennial pack ice in the southern Beaufort Sea was not as it appeared in the summer of 2009. *Geophysical Research Letters* **36**(24): 1–5. DOI: <http://dx.doi.org/10.1029/2009GL041434>.
- Barber, DG, Massom, RA.** 2007. A bi-polar assessment of modes of polynya formation, in Smith, WO, Barber, DG eds., *Polynyas: Windows to the world's oceans*. Amsterdam, the Netherlands: Elsevier: 1–54.
- Barber, DG, Mccullough, G, Babb, D, Komarov, AS, Candlish, LM, Lukovich, JV, Asplin, M, Prinsenberg, S, Dmitrenko, I, Rysgaard, S.** 2014. Climate change and ice hazards in the Beaufort Sea. *Elementa: Science of the Anthropocene* **2**(1982): 1–13. DOI: <http://dx.doi.org/10.12952/journal.elementa.000025>.
- Barnes, PW, Reimnitz, ERK, Fox, D.** 1982. Ice rafting of fine-grained sediment, a sorting and transport

- mechanism, Beaufort Sea, Alaska. *Journal of Sedimentary Research* **52**(2): 493–502.
- BaySys Collaborators.** 2018. CCGS Amundsen Leg-1 Cruise Report. Available at [https://umanitoba.ca/faculties/environment/departments/ceos/media/BaySys_Amundsen_Cruise_Report_2018\(final_compressed\).pdf](https://umanitoba.ca/faculties/environment/departments/ceos/media/BaySys_Amundsen_Cruise_Report_2018(final_compressed).pdf). Accessed 15 June 2020.
- Bouchard, C, Fortier, L.** 2008. Effects of polynyas on the hatching season, early growth and survival of polar cod *Boreogadus saida* in the Laptev Sea. *Marine Ecology Progress Series* **355**: 247–256. DOI: <http://dx.doi.org/10.3354/meps07335>.
- Bouchard, C, Thorrold, SR, Fortier, L.** 2015. Spatial segregation, dispersion and migration in early stages of polar cod *Boreogadus saida* revealed by otolith chemistry. *Marine Biology* **162**(4): 855–868. DOI: <http://dx.doi.org/10.1007/s00227-015-2629-5>.
- Burt, WJ, Thomas, H, Miller, LA, Granskog, MA, Papakyriakou, TN, Pengelly, L.** 2016. Inorganic carbon cycling and biogeochemical processes in an Arctic inland sea (Hudson Bay). *Biogeosciences* **13**(16): 4659–4671. DOI: <http://dx.doi.org/10.5194/bg-13-4659-2016>.
- Copernicus Climate Change Service Climate Data Store.** 2017. Copernicus Climate Change Service (C3 S) (2017): ERA5: Fifth generation of ECMWF atmospheric reanalyses of the global climate. Available at <https://cds.climate.copernicus.eu/cdsapp#!/home>. Accessed 10 September 2019.
- Dainard, PG, Guéguen, C, Yamamoto-Kawai, M, Williams, WJ, Hutchings, JK.** 2019. Interannual variability in the absorption and fluorescence characteristics of dissolved organic matter in the Canada Basin polar mixed waters. *Journal of Geophysical Research: Oceans* **124**(7): 5258–5269. DOI: <http://dx.doi.org/https://doi.org/10.1029/2018JC014896>.
- Darby, DA.** 2003. Sources of sediment found in sea ice from the western Arctic Ocean, new insights into processes of entrainment and drift patterns. *Journal of Geophysical Research: Oceans* **108**(C8, 3257): 1–10. DOI: <http://dx.doi.org/10.1029/2002JC001350>.
- Darby, DA, Myers, WB, Jakobsson, M, Rigor, I.** 2011. Modern dirty sea ice characteristics and sources: The role of anchor ice. *Journal of Geophysical Research: Oceans* **116**(9). DOI: <http://dx.doi.org/10.1029/2010JC006675>.
- Déry, SJ, Mlynowski, TJ, Hernández-Henríquez, MA, Straneo, F.** 2011. Interannual variability and interdecadal trends in Hudson Bay streamflow. *Journal of Marine Systems* **88**(3): 341–351. DOI: <http://dx.doi.org/10.1016/j.jmarsys.2010.12.002>.
- Desharnais, G.** 2004. *Geochemical constraints on the Tectonomagmatic Evolution of the Fox River Belt, Northeastern Manitoba (NTS 53M15 and 16)*. Winnipeg, Manitoba: Manitoba Industry, Economic Development and Mines, Manitoba Geological Survey.
- Dethleff, D, Rachold, V, Tintelnot, M, Antonow, M.** 2000. Sea-ice transport of riverine particles from the Laptev Sea to Fram Strait based on clay mineral studies. *International Journal of Earth Sciences* **89**(3): 496–502. DOI: <http://dx.doi.org/10.1007/s005310000109>.
- Ehn, JK, Papakyriakou, TN, Barber, DG.** 2008. Inference of optical properties from radiation profiles within melting landfast sea ice. *Journal of Geophysical Research* **113**(C09024). DOI: <http://dx.doi.org/10.1029/2007JC004656>.
- Eicken, H, Gradinger, R, Gaylord, A, Mahoney, A, Rigor, I, Melling, H.** 2005. Sediment transport by sea ice in the Chukchi and Beaufort Seas: Increasing importance due to changing ice conditions? *Deep Sea Research Part II: Topical Studies in Oceanography* **52**(24–26): 3281–3302. DOI: <http://dx.doi.org/10.1016/j.dsr2.2005.10.006>.
- Eicken, H, Reimnitz, E, Alexandrov, V, Martin, T, Kassens, H, Viehoff, T.** 1997. Sea-ice processes in the Laptev Sea and their importance for sediment export. *Continental Shelf Research* **17**(2): 205–233. DOI: [http://dx.doi.org/10.1016/S0278-4343\(96\)00024-6](http://dx.doi.org/10.1016/S0278-4343(96)00024-6).
- Fransson, A, Chierici, M, Anderson, LG, Bussmann, I, Kattner, G, Jones, EP, Swift, JH.** 2001. The importance of shelf processes for the modification of chemical constituents in the waters of the Eurasian Arctic Ocean: Implication for carbon fluxes. *Continental Shelf Research* **21**: 225–242.
- Fransson, A, Chierici, M, Nomura, D, Granskog, MA, Kristiansen, S, Martma, T, Nehrke, G.** 2015. Effect of glacial drainage water on the CO₂ system and ocean acidification state in an Arctic tidewater-glacier fjord during two contrasting years. *Journal of Geophysical Research: Oceans* **120**: 2413–2429. DOI: <http://dx.doi.org/doi:10.1002/2014JC010320>.
- Fransson, A, Chierici, M, Nomura, D, Granskog, MA, Kristiansen, S, Martma, T, Nehrke, G.** 2020. Influence of glacial water and carbonate minerals on wintertime sea-ice biogeochemistry and the CO₂ system in an Arctic fjord in Svalbard. *Annals of Glaciology*: 1–21. DOI: <http://dx.doi.org/https://doi.org/10.1017/aog.2020.52>.
- Frey, K, Eicken, H, Perovich, DK, Grenfell, TC, Light, B, Shapiro, H, Stierle, AP.** 2001. *Heat budget and decay of clean and sediment-laden sea ice off the northern coast of Alaska*. Port and Ocean Engineering in the Arctic Conference (POAC'01) Proceedings. Ottawa, Canada: **3**: 1405–1412.
- Geilfus, NX, Galley, RJ, Crabeck, O, Papakyriakou, T, Landy, J, Tison, JL, Rysgaard, S.** 2015. Inorganic carbon dynamics of melt-pond-covered first-year sea ice in the Canadian Arctic. *Biogeosciences* **12**(6): 2047–2061. DOI: <http://dx.doi.org/10.5194/bg-12-2047-2015>.
- Godin, P, Macdonald, RW, Kuzyk, ZZA, Goñi, MA, Stern, GA.** 2017. Organic matter compositions of rivers draining into Hudson Bay: Present-day trends and potential as recorders of future climate change. *Journal of Geophysical Research: Biogeosciences* **122**(7): 1848–1869. DOI: <http://dx.doi.org/10.1002/2016JG003569>.

- Golovin, P, Dmitrenko, I, Kassens, H, Hölemann, JA.** 1999. Frazil ice formation during the spring flood and its role in transport of sediments to the ice cover, in Heidemarie, K, Bauch, HA, Dmitrenko, IA, Eicken, H, Hubberten, H-W, Melles, M, Thiede, J, Timokhov, L eds., *Land-ocean systems in the Siberian Arctic: Dynamics and history*. Berlin, Germany: Springer-Verlag: 125–140.
- Gradinger, RR, Kaufman, MR, Bluhm, BA.** 2009. Pivotal role of sea ice sediments in the seasonal development of near-shore Arctic fast ice biota. *Marine Ecology Progress Series* **394**: 49–63. DOI: <http://dx.doi.org/10.3354/meps08320>.
- Graham, M, Hop, H.** 1995. Aspects of reproduction and larval biology of Arctic cod (*Boreogadus saida*). *Arctic* **48**(2): 130–135. DOI: <http://dx.doi.org/10.14430/arctic1234>.
- Granskog, MA.** 1999. Baltic Sea ice as a medium for storage of particulate matter and elements. *ICES Journal of Marine Science* **56**: 172–175. DOI: <http://dx.doi.org/10.1006/jmsc.1999.0611>.
- Granskog, MA, Kaartokallio, H, Kuosa, H, Thomas, DN, Vainio, J.** 2006. Sea ice in the Baltic Sea—A review. *Estuarine, Coastal and Shelf Science*. **70**(1–2): 145–160. DOI: <http://dx.doi.org/10.1016/j.ecss.2006.06.001>.
- Granskog, MA, Kaartokallio, H, Thomas, DN, Kuosa, H.** 2005. Influence of freshwater inflow on the inorganic nutrient and dissolved organic matter within coastal sea ice and underlying waters in the Gulf of Finland (Baltic Sea). *Estuarine, Coastal and Shelf Science* **65**(1–2): 109–122. DOI: <http://dx.doi.org/10.1016/j.ecss.2005.05.011>.
- Granskog, MA, Macdonald, RW, Kuzyk, ZZA, Senneville, S, Mundy, CJ, Barber, DG, Stern, GA, Saucier, F.** 2009. Coastal conduit in southwestern Hudson Bay (Canada) in summer: Rapid transit of freshwater and significant loss of colored dissolved organic matter. *Journal of Geophysical Research: Oceans* **114**(8). DOI: <http://dx.doi.org/10.1029/2009JC005270>.
- Guéguen, C, Guo, L, Yamamoto-Kawai, M, Tanaka, N.** 2007. Colored dissolved organic matter dynamics across the shelf-basin interface in the western Arctic Ocean. *Journal of Geophysical Research: Oceans* **112**(5): 1–11. DOI: <http://dx.doi.org/10.1029/2006JC003584>.
- Guéguen, C, Itoh, M, Kikuchi, T, Eert, J, Williams, WJ.** 2015. Variability in dissolved organic matter optical properties in surface waters in the Amerasian Basin. *Frontiers in Marine Science* **2**(78): 1–9. DOI: <http://dx.doi.org/10.3389/fmars.2015.00078>.
- Haraldsson, C, Anderson, LG, Hassellöv, M, Hulth, S, Olsson, K.** 1997. Rapid, high-precision potentiometric titration of alkalinity in ocean and sediment pore waters. *Deep Sea Research Part I: Oceanographic Research Papers* **44**(12): 2031–2044. DOI: [http://dx.doi.org/10.1016/S0967-0637\(97\)00088-5](http://dx.doi.org/10.1016/S0967-0637(97)00088-5).
- Harasyn, ML, Isleifson, D, Barber, DG.** 2019. The influence of surface sediment presence on observed passive microwave brightness temperatures of first year sea ice during the summer melt period. *Canadian Journal of Remote Sensing* **45**(3–4): 1–17. Taylor & Francis. DOI: <http://dx.doi.org/10.1080/07038992.2019.1625759>.
- Héquette, A, Tremblay, P, Hill, PR.** 1999. Nearshore erosion by combined ice scouring and near-bottom currents in eastern Hudson Bay, Canada. *Marine Geology* **158**(1): 253–266. DOI: [http://dx.doi.org/10.1016/S0025-3227\(98\)00164-9](http://dx.doi.org/10.1016/S0025-3227(98)00164-9).
- Hochheim, KP, Barber, DG.** 2014. An update on the ice climatology of the Hudson Bay system. *Arctic, Antarctic, and Alpine Research* **46**(1): 66–83. DOI: <http://dx.doi.org/10.1657/1938-4246-46.1.66>.
- Hornby, C, Ehn, J, Matthes, L, Blondeau, S, Basu, A, Goharrokhi, M, Karmiruk, Z, Kirillov, S.** 2016. BaySys 2016 Mooring Program Cruise Report. Winnipeg, Manitoba. Available at <http://hdl.handle.net/1993/33754>. Accessed 15 June 2020.
- Huck, P, Light, B, Eicken, H, Haller, M.** 2007. Mapping sediment-laden sea ice in the Arctic using AVHRR remote-sensing data: Atmospheric correction and determination of reflectances as a function of ice type and sediment load. *Remote Sensing of Environment* **107**(3): 484–495. DOI: <http://dx.doi.org/10.1016/j.rse.2006.10.002>.
- Ito, M, Ohshima, KI, Fukamachi, Y, Hirano, D, Mahoney, AR, Jones, J, Takatsuka, T, Eicken, H.** 2019. Favorable conditions for suspension freezing in an arctic coastal polynya. *Journal of Geophysical Research: Oceans* **124**(12): 8701–8719. DOI: <http://dx.doi.org/10.1029/2019JC015536>.
- Kempema, EW, Reimnitz, E, Barnes, PW.** 1989. Sea ice sediment entrainment and rafting in the Arctic. *Journal of Sedimentary Research* **59**(2): 308–317.
- Kirillov, S, Babb, D, Dmitrenko, I, Landy, J, Lukovich, J, Ehn, J, Sydor, K, Barber, D, Stroeve, J.** 2020. Atmospheric forcing drives the winter sea ice thickness asymmetry of Hudson Bay. *Journal of Geophysical Research: Oceans* **125**(2). DOI: <http://dx.doi.org/10.1029/2019JC015756>.
- Krumpen, T, Belter, HJ, Boetius, A, Damm, E, Haas, C, Hendricks, S, Nicolaus, M, Nöthig, E, Paul, S, Peeken, I, Ricker, R.** 2019. Arctic warming interrupts the Transpolar Drift and affects long-range transport of sea ice and ice-rafted matter. *Scientific Reports* **9**(1): 1–9. DOI: <http://dx.doi.org/10.1038/s41598-019-41456-y>.
- Kuzyk, ZZA, Goñi, MA, Stern, GA, Macdonald, RW.** 2008a. Sources, pathways and sinks of particulate organic matter in Hudson Bay: Evidence from lignin distributions. *Marine Chemistry* **112**(3–4): 215–229. DOI: <http://dx.doi.org/10.1016/j.marchem.2008.08.001>.
- Kuzyk, ZZA, Macdonald, RW, Granskog, MA, Scharien, RK, Galley, RJ, Michel, C, Barber, DG, Stern, GA.** 2008b. Sea ice, hydrological, and biological processes in the Churchill River estuary region, Hudson Bay. *Estuarine Coastal and Shelf Science* **77**(3): 369–

384. DOI: <http://dx.doi.org/10.1016/j.ecss.2007.09.030>.
- Kuzyk, ZZA, Macdonald, RW, Johannessen, SC, Gobeil, C, Stern, GA.** 2009. Towards a sediment and organic carbon budget for Hudson Bay. *Marine Geology* **264**(3–4): 190–208. DOI: <http://dx.doi.org/10.1016/j.margeo.2009.05.006>.
- Kwok, R, Cunningham, G, Markus, T, Hancock, D, Morison, JH, Palm, SP, Farrell, SL, Ivanoff, A, Wimert, J, Team Ices-2 S.** 2019a. ATLAS/ICESat-2 L3A sea ice freeboard, Version 2. Boulder, CO. DOI: <http://dx.doi.org/https://doi.org/10.5067/ATLAS/ATL10.002>.
- Kwok, R, Markus, T, Kurtz, NT, Petty, AA, Neumann, TA, Farrell, SL, Cunningham, GF, Hancock, DW, Ivanoff, A, Wimert, JT.** 2019b. Surface height and sea ice freeboard of the arctic ocean from ICESat-2: Characteristics and early results. *Journal of Geophysical Research: Oceans* **124**(10): 6942–6959. DOI: <http://dx.doi.org/10.1029/2019JC015486>.
- Landy, JC, Ehn, JK, Babb, DG, Thériault, N, Barber, DG.** 2017. Sea ice thickness in the Eastern Canadian Arctic: Hudson Bay Complex and Baffin Bay. *Remote Sensing of Environment* **200**: 281–294. DOI: <http://dx.doi.org/10.1016/j.rse.2017.08.019>.
- Larssen, BB, Elverhøi, A, Aagaard, P.** 1987. Study of particulate material in sea ice in the Fram Strait—A contribution to paleoclimatic research? *Polar Research* **5**: 313–315.
- Lavoie, D, Pinet, N, Dietrich, J, Chen, Z.** 2015. The Paleozoic Hudson Bay Basin in northern Canada: New insights into hydrocarbon potential of a frontier intracratonic Basin. *American Association of Petroleum Geologists Bulletin* **99**(5): 859–888. DOI: <http://dx.doi.org/10.1306/12161414060>.
- Ledley, TS, Pfirman, S.** 1997. The impact of sediment-laden snow and sea ice in the Arctic on climate. *Climatic Change* **37**(4): 641–664. DOI: <http://dx.doi.org/10.1023/A:1005354912379>.
- Light, B, Maykut, GA, Grenfell, TC.** 1998. The effect of included particulates on the spectral albedo of sea ice. *Journal of Geophysical Research: Oceans* **103**(C12): 27739–27752.
- Macdonald, R, Paton, D, Carmack, E, Omstedt, A.** 1995. The freshwater budget and under-ice spreading of Mackenzie River water in the Canadian Beaufort Sea based on salinity and $^{18}\text{O}/^{16}\text{O}$ measurements in water and ice. *Journal of Geophysical Research: Oceans* **100**(C1): 895–919. DOI: <http://dx.doi.org/10.1029/94JC02700>.
- Materials Data Incorporated.** 2012. JADE Pro (Computer Software). Livermore, CA.
- Miller, MC, McCave, IN, Komar, PD.** 1977. Threshold of sediment motion under unidirectional currents. *Sedimentology* **24**: 507–527.
- Moore, K, Fayek, M, Lemes, M, Rysgaard, S, Holländer, HM.** 2017. Fractionation of hydrogen and oxygen in artificial sea ice with corrections for salinity for determining meteorological water content in bulk ice samples. *Cold Regions Science and Technology* **142**: 93–99. DOI: <http://dx.doi.org/10.1016/j.coldregions.2017.07.011>.
- Nomura, D, Nishioka, J, Granskog, MA, Krell, A, Matoba, S, Toyota, T, Hattori, H, Shirasawa, K.** 2009. Nutrient distributions associated with snow and sediment-laden layers in sea ice of the southern Sea of Okhotsk. *Marine Chemistry* **119**: 1–8. DOI: <http://dx.doi.org/10.1016/j.marchem.2009.11.005>.
- Nurnberg, D, Wollenburg, I, Dethleff, D, Eicken, H, Kassens, H, Letzig, T, Reimnitz, E.** 1994. Sediments in Arctic sea ice: Implications for entrainment, transport and release. *Marine Geology* **119**: 185–214.
- O’Keefe, A, Deacon, DAG.** 1988. Cavity ring-down optical spectrometer for absorption measurements using pulsed laser sources. *Review of Scientific Instruments* **59**(12): 2544–2551. DOI: <http://dx.doi.org/10.1063/1.1139895>.
- Pelletier, BR.** 1986. Seafloor morphology and sediments, in Martini IP eds., *Canadian inland seas* (Elsevier oceanography series; vol. 44). New York, NY: Elsevier : 143–162.
- Perovich, DK, Roesler, CS, Pegau, WS.** 1998. Variability in Arctic sea ice optical properties. *Journal of Geophysical Research: Oceans* **103**(C1): 1193–1208.
- Petrusevich, VY, Dmitrenko, IA, Niemi, A, Kirillov, SA, Kamula, CM, Kuzyk, ZZA, Barber, DG, Ehn, JK.** 2020. Impact of tidal dynamics on diel vertical migration of zooplankton in Hudson Bay. *Ocean Science* **16**: 337–353.
- Pfirman, S.** 1987. Sediment distribution of the Greenland Sea and the Fram Strait. *Polar Research* **5**(3): 319–320. DOI: <http://dx.doi.org/10.1111/j.1751-8369.1987.tb00563.x>.
- Pfirman, S, Lange, M, Wollenburg, I, Schlosser, P.** 1990. Sea ice characteristics and the role of sediment inclusions in deep-sea deposition: Arctic–Antarctic comparisons, in Bleil, U, Thiede, J eds., *Geological history of the polar oceans: Arctic versus Antarctic*. The Netherlands: Kluwer Publishing: 187–211.
- Pfirman, S, Mainz, L, Lange, MA.** 1989. Lithogenic sediment on Arctic pack ice: Potential Aeolian flux and contribution to deep sea sediments, in Leinen, M, Sarnthein, M eds., *Paleoclimatology and paleometeorology: Modern and past patterns of global atmospheric transport*. Dordrecht, the Netherlands: Springer: 463–493. DOI: <http://dx.doi.org/10.1007/978-94-009-0995-3>.
- Redfield, A, Friedman, I.** 1969. The effect of meteoric water, melt water and brine on the composition of Polar Sea water and of the deep waters of the ocean. *Deep-Sea Research* **16**(suppl): 197–214.
- Reimnitz, E, Kempema, EW, Barnes, PW.** 1987. Anchor ice, seabed freezing, and sediment dynamics in shallow Arctic seas. *Journal of Geophysical Research: Oceans* **92**(C13): 671–678.
- Reimnitz, E, Marincovich, L, McCormick, M, Briggs, WM.** 1992. Suspension freezing of bottom sediment and biota in the Northwest Passage and implications for Arctic Ocean sedimentation. *Canadian Journal of*

- Earth Sciences* **29**(4): 693–703. DOI: <http://dx.doi.org/10.1139/e92-060>.
- Reimnitz, E, McCormick, M, McDougall, K, Brouwers, E.** 1993. Sediment export by ice rafting from a coastal polynya, Arctic Alaska. *USA. Arctic and Alpine Research* **25**(2): 83–98. DOI: <http://dx.doi.org/10.2307/1551544>.
- Rösel, A, Kaleschke L, Birnbaum, G.** 2012. Melt ponds on Arctic sea ice determined from MODIS satellite data using an artificial neural network. *Cryosphere* **6**(2): 431–446. DOI: <http://dx.doi.org/10.5194/tc-6-431-2012>.
- Rosenberg, DM, Chambers, PA, Culp, JM, Franzin, WG, Nelson, PA, Salki, AG, Stainton, MP, Bodaly, RA, Newbury, RW.** 2005. Nelson and Churchill river basins, in Benke AC, Cushing CE eds., *Rivers of North America*. Burlington, MA: Elsevier: 853–902.
- Rysgaard, S, Glud, RN, Sejr, MK, Bendtsen, J, Christensen, PB.** 2007. Inorganic carbon transport during sea ice growth and decay: A carbon pump in polar seas. *Journal of Geophysical Research: Oceans* **112**(C03016). DOI: <http://dx.doi.org/10.1029/2006JC003572>.
- Skoog, A, Hall, PO., Hulth, S, Paxéus, N, Loeff V Der, Rutgers, M, Westerlund, S.** 1996. Early diagenetic production and sediment-water exchange of fluorescent dissolved organic matter in the coastal environment. *Geochimica et Cosmochimica Acta* **60**(19): 3619–3629. Available at papers2://publication/uuid/86B3A45B-DBD7-4628-A1C7-E7906626A36B.
- Tan, F, Strain, P.** 1996. Sea ice and oxygen isotopes in Foxe Basin, Hudson Bay, and Hudson Strait, Canada. *Journal of Geophysical Research: Oceans* **101**(C9): 20869–20876. DOI: <http://dx.doi.org/10.1029/96JC01557>.
- Tank, SE, Raymond, PA, Striegl, RG, McClelland, JW, Holmes, RM, Fiske, GJ, Peterson, BJ.** 2012. A land-to-ocean perspective on the magnitude, source and implication of DIC flux from major Arctic rivers to the Arctic Ocean. *Global Biogeochemical Cycles* **26**(4): 1–15. DOI: <http://dx.doi.org/10.1029/2011GB004192>.
- Thomas, DN, Papadimitriou, S, Michel, C.** 2010. Biogeochemistry of sea ice, in Thomas DN, Dieckmann GS eds., *Sea ice*. Oxford, UK: Wiley-Blackwell: 425–467. DOI: http://dx.doi.org/10.1007/978-90-481-2642-2_639.
- Timco GW, Weeks WF.** 2010. A review of the engineering properties of sea ice. *Cold Regions Science and Technology* **60**: 107–129. DOI: <http://dx.doi.org/10.1016/j.coldregions.2009.10.03>.
- Toyota, T, Smith, IJ, Gough, AJ, Langhorne, PJ, Leonard, GH, Van Hale, RJ, Mahoney, AR, Haskell, TG.** 2013. Oxygen isotope fractionation during the freezing of sea water. *Journal of Glaciology* **59**(216): 697–710. DOI: <http://dx.doi.org/10.3189/2013JG12J163>.
- Varpe, Ø, Daase, M, Kristiansen, T.** 2015. A fish-eye view on the new Arctic lightscape. *ICES Journal of Marine Science* **72**: 2532–2538.
- Wegner, C, Wittbrodt, K, Hölemann, JA, Janout, MA, Krumpfen, T, Selyuzhenok, V, Novikhin, A, Polyakova, Y, Krykova, I, Kassens, H, Timokhov L.** 2017. Sediment entrainment into sea ice and transport in the Transpolar Drift: A case study from the Laptev Sea in winter 2011/2012. *Continental Shelf Research* **141**: 1–10. DOI: <http://dx.doi.org/10.1016/j.csr.2017.04.010>.
- Yamamoto-Kawai, M, McLaughlin, FA, Carmack, EC, Nishino, S, Shimada, K.** 2009. Aragonite undersaturation in the Arctic Ocean: Effects of ocean acidification and sea ice melt. *Science* **326**(5956): 1098–1100. DOI: <http://dx.doi.org/10.1126/science.1174190>.

How to cite this article: Barber, DG, Harasyn, ML, Babb, DG, Capelle, D, McCullough, G, Dalman, LA, Matthes, LC, Ehn, JK, Kirillov, S, Kuzyk, Z, Basu, A, Fayak, M, Schembri, S, Papkyriakou, T, Ahmed, MMM, Else, B, Guéguen, C, Meilleur, C, Dmitrenko, I, Mundy, CJ, Gupta, K, Rysgaard, S, Stroeve, J, Sydor, K. 2021. Sediment-laden sea ice in southern Hudson Bay: Entrainment, transport, and biogeochemical implications. *Elementa: Science of the Anthropocene* 9(1). DOI: <https://doi.org/10.1525/elementa.2020.00108>

Domain Editor-in-Chief: Jody W. Deming, University of Washington, Seattle, WA, USA

Associate Editor: Stephen F. Ackley, Department of Geological Sciences, University of Texas at San Antonio, San Antonio, TX, USA

Knowledge Domain: Ocean Science

Part of an Elementa Special Feature: BaySys

Published: May 21, 2021 **Accepted:** April 12, 2021 **Submitted:** July 21, 2020

Copyright: © 2021 The Author(s). This is an open-access article distributed under the terms of the Creative Commons Attribution 4.0 International License (CC-BY 4.0), which permits unrestricted use, distribution, and reproduction in any medium, provided the original author and source are credited. See <http://creativecommons.org/licenses/by/4.0/>.



Elem Sci Anth is a peer-reviewed open access journal published by University of California Press.

OPEN ACCESS The Open Access logo, consisting of the words "OPEN ACCESS" followed by a circular icon containing a stylized padlock with an open keyhole.